Reprocessing of legacy seismic reflection profile data and its implications for plate flexure in the vicinity of the Hawaiian Islands

P. Cilli[1], A. B. Watts[1], B. Boston[2], D. J. Shillington[3]

[1]Department of Earth Sciences, University of Oxford, Oxford, UK.

[2*]Lamont Doherty Earth Observatory of Columbia University, Palisades, NY, USA.

[3]School of Earth and Sustainability, Northern Arizona University, Flagstaff, AZ, USA.

Submitted to Journal Geophysical Research

*Now at Department of Geosciences, Auburn University, Auburn, AL, USA.

Abstract

During 1975-1988, an academic research ship, R/V *Robert D. Conrad*, acquired more than 150,000-line-km of multichannel seismic reflection profile data from each of the world's main ocean basins and their margins. This extensive legacy seismic data set, which involved both single ship and two-ship data acquisition, has been widely used by the marine geoscience community. We report on our experience in reprocessing seismic reflection profile data acquired during *Conrad* cruise RC2308 to the Hawaiian Islands region in August/September 1982. We show that the application of modern, industry standard processing techniques, including de-noise, de-bubble, deconvolution and migration, can significantly enhance 40+ year old legacy seismic reflection profile data. The reprocessed data reveals more precisely, and with much less scatter, the flexure of Cretaceous Pacific oceanic crust caused by the Pliocene-Recent volcanic loads that comprise the Hawaiian Islands. A comparison of observed picks of top oceanic crust which has been corrected for the Hawaiian swell and the Molokai Fracture Zone with the calculations of a simple 3-dimensional elastic plate (flexure) model reveals a best fit elastic plate thickness of the lithosphere, T_e, of 26.7 km, an average infill density of 2701 kg m^{-3}, and a Root Mean Square (RMS) difference between observations and calculations of 305 m. Tests show these results depend weakly on the load density assumed and that the average infill density is close to what would be predicted from an arithmetic average of the flanking moat infill density and the infill density that immediately underlies the volcanic edifice.

Plain Language summary

The mid-1970s to mid-1980s saw a rapid increase in the acquisition of marine seismic reflection profile data by academic research vessels using large airgun arrays and long multichannel streamers. The data have provided some of the best images we have of the structure of mid-ocean ridges, transform faults and fracture zones and deep-sea trenches; however, the processing of these data was rudimentary in comparison to modern standards. We show here how reprocessing of seismic reflection profile data acquired some 40+ years ago in the vicinity of the Hawaiian Islands that utilize modern methods of denoise (we use the term 'denoise' here and elsewhere to collectively describe basic processing steps such as trace edits, Bandpass filtering and FX Swell noise removal in the shot and channel domains),

deconvolution, and migration technologies have significantly improved imaging of the top and bottom of oceanic crust, reducing the scatter in reflector depths from a legacy data set by almost a factor of two. This, in turn, has led to improved resolution of the large-scale deformation caused by the individual volcano loads that comprise the Hawaiian Islands and, since the ages of these loads and the ocean floor on which these loads have been emplaced are known, to a better understanding of the stress state, strength and rheological properties of Earth's tectonic plates.

Introduction

Seismic reflection profiling is one of the principal methods with which we can image the deep structure of Earth's crust and upper mantle. During 1975-1988, the research vessel *Robert D. Conrad*, owned by the US Navy and operated by the Lamont-Doherty Geological Observatory of Columbia University, acquired more than 150,000-line km of marine geophysical data, including MultiChannel Seismic (MCS) reflection profile data, during 31 approximately 30-day-long cruises to the Atlantic, Indian and Pacific Ocean basins and their margins. This extensive legacy seismic data set, which involved both single and two-ship experiments, has been widely used by the marine geoscience community to determine sediment thickness in the deep oceans (e.g., Sheridan et al., 1978), to image the velocity structure and Moho of oceanic crust at mid-ocean ridges (e.g., Vera and Diebold, 1994), fracture zones (e.g., Minshull et al., 1991) and active (e.g., Lewis and Hayes, 1989) and passive continental margins (e.g., Mutter et al., 1984), and to constrain processes of oceanic crustal accretion (e.g., Detrick et al., 1987) and subduction (e.g., Bangs and Cande, 1997) and models for the thermal and mechanical evolution of oceanic lithosphere (e.g., Watts et al., 1985; Wessel, 1993) and the rheological laws that describe brittle deformation and ductile flow at lithospheric conditions (e.g., Zhong and Watts, 2013).

The *Conrad* MCS data were usually processed at Lamont-Doherty Geological Observatory using 'in-house' software within a few years of its acquisition, but with few exceptions have not been reprocessed since then. Although the data set was acquired with the latest technology available to academia at the time, many cruises lacked a near-field hydrophone and tuned air-gun arrays. This led to significant issues in the processing, and imaging, for example in removal of bubble pulse reverberations. Furthermore, processing was based on 'in-house' computer software that focussed on de-noise, filtering, and velocity

106 analysis, which was simple by today's standards. Since the late 1980s, however, there has been
107 considerable progress in the development of software for the processing of seismic reflection
108 profile data. Today, industry-standard software is widely available in academia which utilises
109 an array of sophisticated processing and imaging algorithms including de-noise, de-bubble,
110 deconvolution and many different time and depth migration techniques (e.g., Yilmaz, 2001).
111
112 The purpose of this paper is to present the results of reprocessing of the *Conrad* MCS
113 data acquired some 40 years ago during a single- and two-ship seismic experiment in the
114 vicinity of the Hawaiian Islands, central Pacific Ocean. We show that reprocessing using
115 modern techniques can considerably enhance a legacy seismic data set to the extent that it
116 improves the signal to noise ratio of the data and improves geological interpretation. The results
117 of our work have implications for the many other seismic data sets acquired on *Conrad*. In
118 particular, undertaking reanalysis of these legacy datasets with modern methods is important
119 given the complexities today of acquiring deep seismic data due, for example, to the
120 establishment of marine conservation areas, ambiguities in offshore territorial claims, and the
121 possible effect of the seismic source on marine mammals and their habitats. The results of this
122 reprocessing also enable new insights into the crustal structure of the hotspot generated
123 Hawaiian Ridge and the oceanic lithosphere on which it was constructed.

124 ***Conrad* RC2308 cruise**

125 During August/September 1982, the US Navy owned, and Lamont-Doherty Geological
126 Observatory of Columbia University operated research vessel R/V *Robert D. Conrad*, acquired
127 approximately 5484-line km of MCS data along three transects which intersected the Hawaiian
128 Ridge between the islands of Oahu and Molokai and Oahu and Kauai (Fig. 1). The *Conrad* was
129 equipped during the experiment with a 2 × 1000 cu. in. (16.4 l) and 1 × 466 cu. in. (7.6 l) Bolt
130 air gun array, a Seismic Engineering 3.6-km-long analogue hydrophone streamer, a Bell
131 Aerospace BGM-3 air-sea gravimeter and a Loran C and Magnavox satellite navigation system.

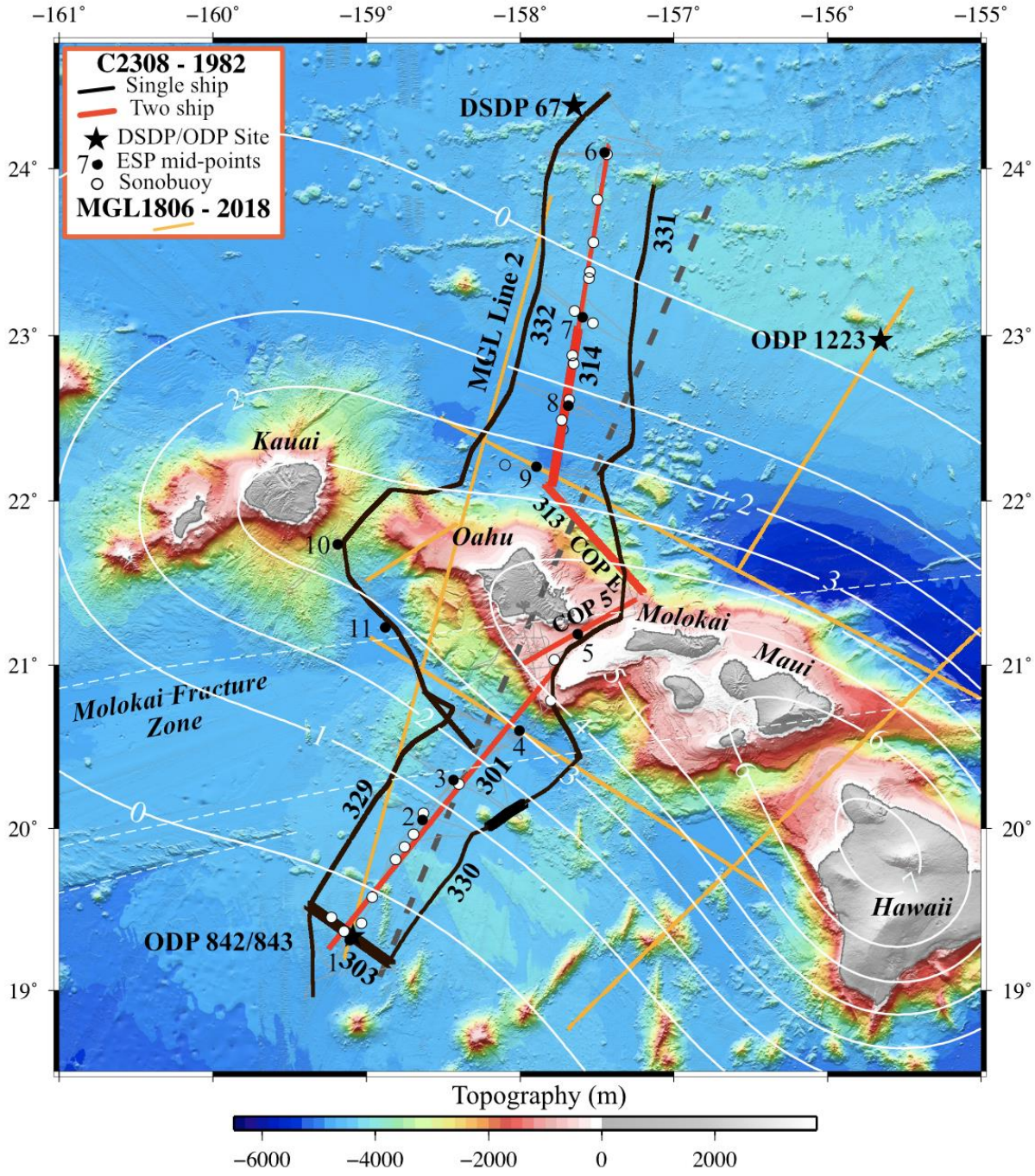

Figure 1. Location map of the Hawaiian Islands region showing the Multi-Channel Seismic (MCS) reflection profiles acquired during R/V *Robert D. Conrad* Cruise RC2308 (solid black and red lines) together with the newly acquired MCS data during R/V *Marcus G. Langseth* cruise MGL1806 (solid orange lines). Thick lines locate the segments of MCS data shown along Lines 303, 314, 313 COP E and 330 in Fig. 7, 8, 9 and 10 respectively. Filled black circles (with number) show ESP mid-points. Filled white circles show sonobuoys deployed during the experiment that recorded refractions. Dashed grey line shows the profile along which the velocity data acquired at ESP mid-points was projected. Bathymetry is based on a 1 × 1 minute grid of GEBCO single beam echo-sounder and multibeam (swath) data plus NASA Shuttle Radar Topography (SRTM 2020) data. Thin dashed white lines locate the strands of the Molokai Fracture Zone (MFZ) as digitised by Mathews et al. (2011). Solid white lines show the calculated flexure of the lithosphere (contour interval = 1 km) due to the

surface load of the Hawaiian Islands, assuming an effective elastic thickness of the lithosphere, T_e, of 30 km.

The orientation of the 3 transects, shown in Fig. 1, was designed to cross the calculated flexural depression, and flanking moats and bulges at a high angle. The "central" transect (i.e., labelled Lines 301 and 314 in Fig. 1) was a two-ship experiment that involved *Conrad* and a second ship, R/V *Kana Keoki* from the University of Hawaii which was equipped with a source array comprised of 1 × 1000 cu. in and 2 × 466 cu. in. airguns. During the experiment, the lead ship, *Kana Keoki*, was separated from *Conrad* by a constant offset which was continuously monitored using a Miniranger/Raydist system (Fig. 2). Constant bearings of the *Kana Keoki* were recorded on Conrad's Bridge to ensure the two ships maintained a constant offset. *Conrad* and *Kana Keoki* shot on alternate half minutes into Conrad's streamer.

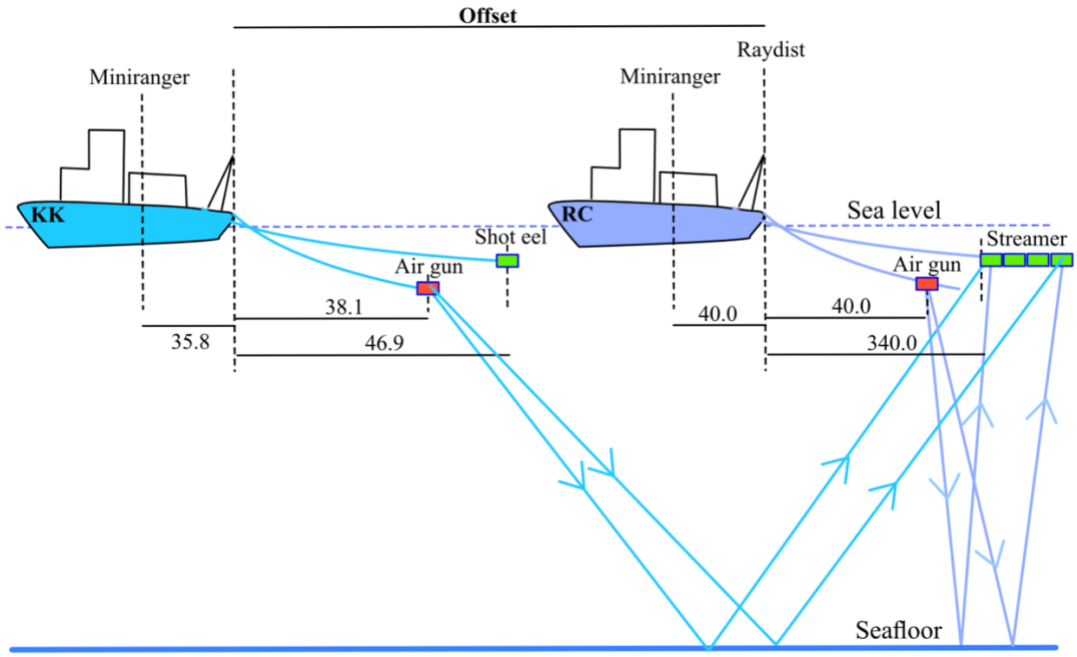

Figure 2. Schematic diagram showing the geometry of data acquisition during the two-ship experiment. Also shown is the ray path of a seafloor reflected arrival generated by each ship firing alternately into the head and tail active section of Conrad's streamer.

"Constant Offset Profiles" (COPs) were acquired to the south and north of Oahu along the central transect. The southern part of the central transect was made up of a southbound COP A at an offset of 3.6 km and northbound COPs B, C and D (Fig. 3) at an offset of 16 km. The northern part of the central transect was made up of a northbound COP F at an offset of 3.6 km and southbound COPs G, H and I (Fig. 4) at an offset of 16 km. The 16 km offset was selected at sea based on disposable sonobuoy data (open circles in Fig. 1), which showed strong, well-defined, sub-critical reflections at this range. The reflection data acquired with this novel two-

ship configuration resulted in the equivalent of data acquired from a single ship with a long streamer and high receiver density.

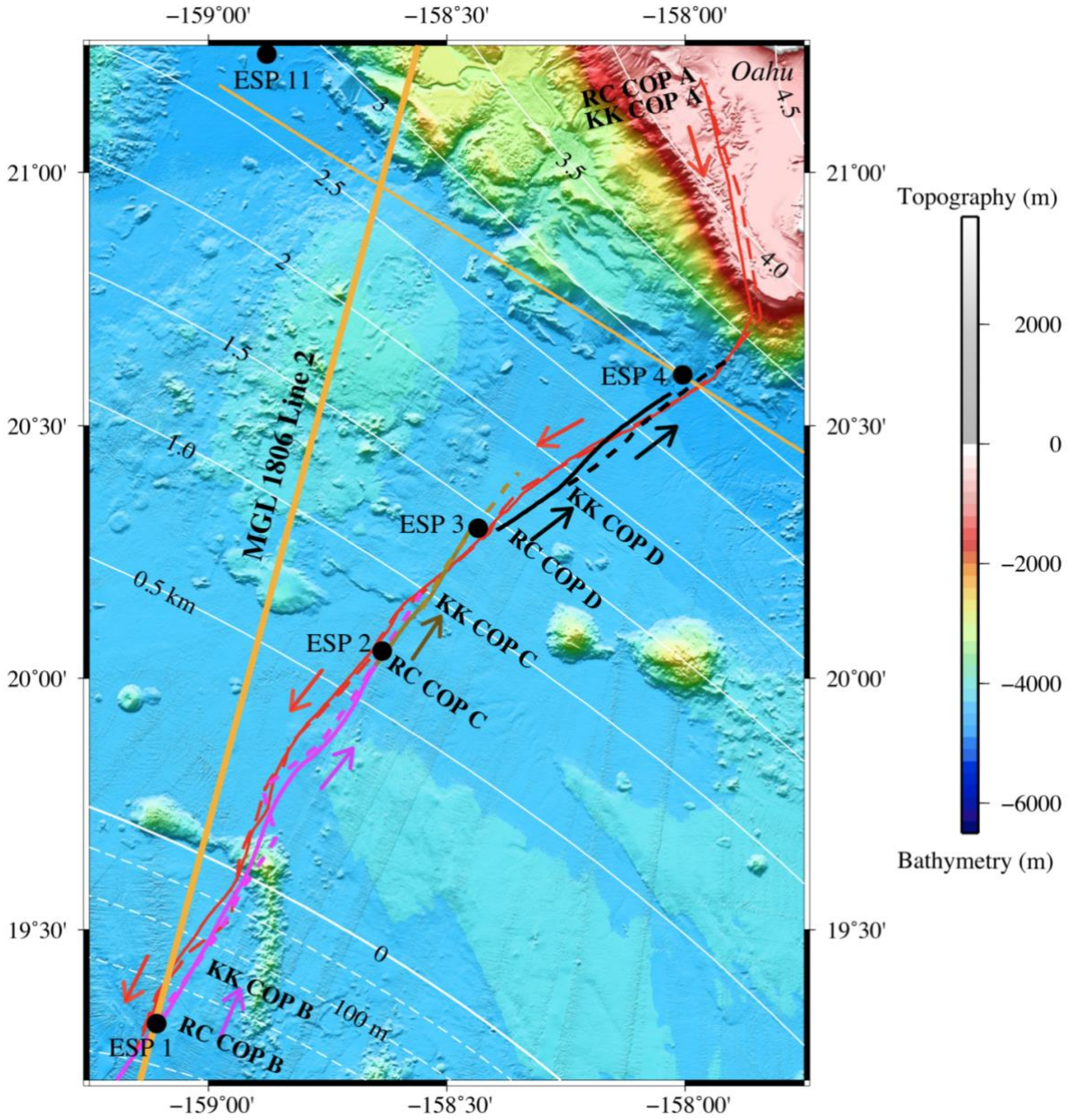

Figure 3. The two-ship experiment south of Oahu which comprised an "outgoing" (i.e., southbound) Constant Offset Profile (COP) A (red solid line) at a ship separation of 3.6 km and "ingoing" (i.e., northbound) COPs B (purple solid line), C (brown solid line) and D (black solid line) at a ship separation of 16 km. Filled black circles show ESP mid-points. RC = *Robert D. Conrad* (solid lines). KK = *Kana Keoki* (dashed lines). White solid lines show the flexural depression at 0.5 km interval for the same value of the elastic thickness as used in Fig. 1. White dashed lines show the flexural bulge at 50 m interval.

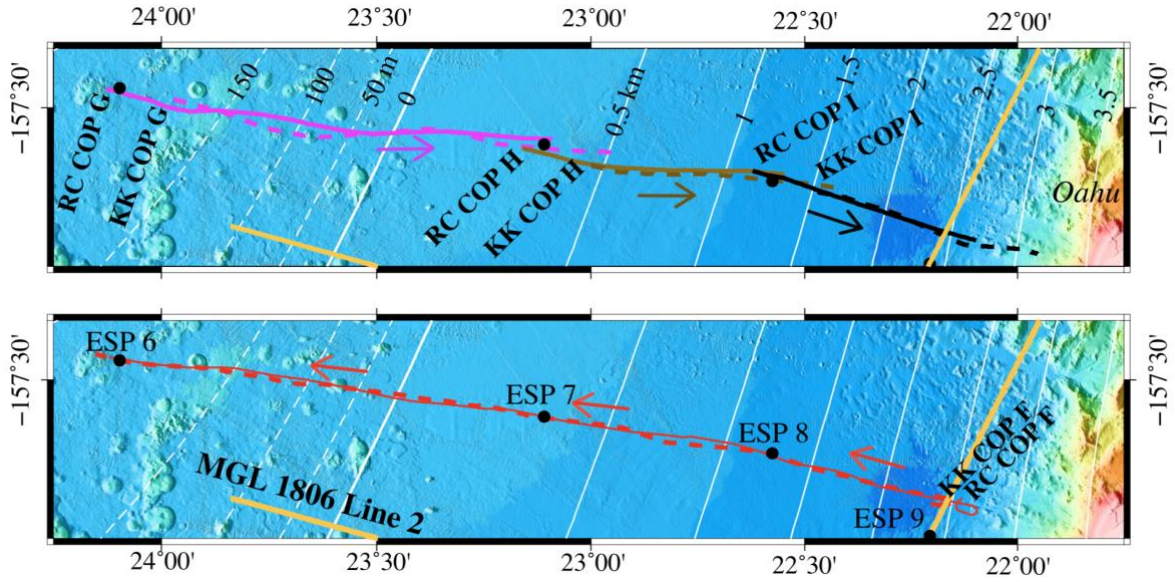

Figure 4. The two-ship experiment north of Oahu which comprised an "outgoing" (i.e., northbound) Constant Offset Profile (COP) F at a ship separation of 3.6 km and "ingoing" (i.e., southbound) COPs G, H, and I at a ship separation of 16 km. White lines are as defined in Fig. 3.

In between the northbound COPs B, C, and D south of Oahu and southbound COPs G, H, and I north of Oahu, Expanding Spread Profile (ESP) seismic refraction data were acquired during which the two ships separated in opposite directions from a mid-point (Figs. 3,4) to an end point about 60 km from the mid-point. At the end points each ship turned on a reciprocal course and approached each other. During the "outgoing" segment *Kana Keoki* fired its airguns at 1 minute interval and *Conrad* received while during the "incoming" segment *Conrad* fired its airguns at 1 minute interval with every 10th minute missing and *Kana Keoki* fired its explosive charges at 10-minute intervals. This ESP data, together with sonobuoy data, provided the necessary *P* wave velocity data for converting the recorded MCS reflection profile data from travel time to depth.

The western and eastern transects (i.e., Lines 329, 330, 331 and 332 in Fig. 1) were a single ship experiment in which *Conrad* acquired MCS data along lines connecting the ESP end points. During this part of the experiment Conrad shot to its 3.6-km-long streamer at 20 s intervals with a recording length of 12 s.

Data from the two-ship and single ship experiments were recorded on each of the 48 channels of Conrad's streamer which, in turn, were logged on a Texas Instrument DFS IV on 1600 DPI 9-track tape with a 4- or 8-ms sampling rate and recording lengths of 20, 39 and 12

s for the COP, ESP and CDP part of the experiment respectively. There were a total of ~43,250 shots, resulting in 867 9-track tapes and approximately 20-GB of digital data.

Seismic Data Reprocessing

In 2016 Lamont-Doherty Earth Observatory entered into an agreement with ION Geophysical in Houston, Texas to convert all the 9-track MCS data tapes acquired on *Conrad* to a standard SEGY format (S. Carbotte, pers. comm). The digitised data for the *Conrad* RC2308 cruise was released early by ION so that it could be used for ship track planning for the R/V *Marcus G. Langseth* MGL1806 seismic reflection and refraction cruise (Dunn et al., 2019; Boston et al., 2019) which took place during April/June 2018.

The first step in the reprocessing was to generate the navigation data and merge it with the digitised legacy gathers. Using the navigation data recorded on the *Conrad* and *Kana Keoki*, as well as the idealised acquisition geometry shown in Fig. 2, we created a nominal survey geometry for all seismic lines, including an estimated X-Y pair for all shots, receivers, and CMP locations.

The northern and southern parts of the central transect (Figs. 3,4) consisted of 8 COPs and so were processed as two separate composite lines: Line 301 south of Oahu and Line 314 north of Oahu. The processing flow for each line consisted of loading the four individual SEGY files into the Shearwater Geoservices Ltd *Reveal* processing software and performing trace edits and quality control. The four seismic volumes were then merged into one for the remainder of the processing. At this point, source and receiver depth headers were assigned and the data was gridded to the nominal line geometry, calculating midpoint locations from the ship's navigation for each source-receiver pair. The midpoints were then projected onto a line or curve for reprocessing.

Pre-processing involved a 5 Hz low-cut filter, F-X swell noise removal in the shot then channel domain, self-consistent amplitude corrections, and Surface-Related Multiple Attenuation (SRMA) (Fig. 5). The subsequent deconvolution process was focussed primarily on bubble pulse removal due to the strong bubble pulse present in the source signature.

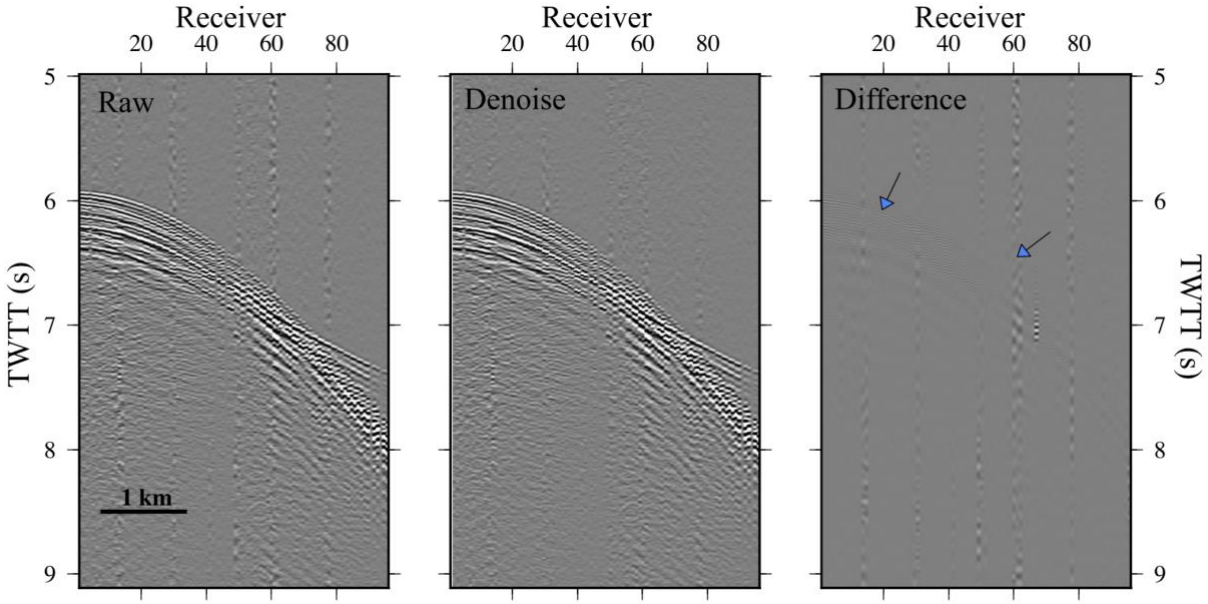

Figure 5. An example of conservative denoising applied to a 'shot' gather (FFID 2499) from *Conrad* and *Kana Keoki* alternately shooting into *Conrad*'s streamer along Line 301 in the flexural moat south of Oahu, showing before (left) and after (middle) denoise, as well as their difference (right). Pre-processing shown includes low-cut filtering, F-X swell removal in shot and channel domain, self-consistent amplitude correction, and SRMA (water bottom multiple not visible). Accordingly, some low frequency bubble noise (left arrow) is removed as well as swell and other noise (right arrow). The gather shows reflections from the seafloor and from sediments in the sub-seafloor and a refraction emerging at offsets of ~2.2 km and greater.

Velocity models were created for processing and imaging after preliminary pre-processing (low-cut filter and swell noise reduction) was performed. The centre point for ESP 1-9 *P* wave velocities were located along the central transect (Fig 1, red lines) while ESPs 10 and 11 were located on the western transect (Fig 1, Line 332). Therefore, the velocity model for the central and eastern transects (Fig 1, Lines 301, 314, COP 5, COP E, 330, and 331) was built using velocities from only ESPs 1-9. The original ESP digital seismic data was unavailable for reinterpretation, so rather than re-deriving ESP velocities from the seismic data, we used the original interpretations reported in the literature by Watts et al. (1985), ten_Brink, (1986), Brocher and ten Brink (1987), ten Brink and Brocher (1987), Lindwall (1988a, 1988b).

To generate a velocity model that spanned the central and eastern transects, the midpoint locations of ESPs 1-9 were projected onto a central line passing through Oahu (Fig. 1, dashed grey line). We chose this line because it is approximately perpendicular to the local trend of the Hawaiian Ridge and was used to project the RC2308 gravity, bathymetry, and legacy interpretations (referred to as "picks" in this paper) of the seismic data in Watts et al., (1985) and Watts and ten Brink (1989). All the ESP mid-point *P* wave velocities were available as a function of depth below the seafloor and so were resampled with linear interpolation onto

a regular, finely spaced depth grid before smoothing was applied. After this, interpolation between the depth-gridded velocity trends was performed along the line of projection, creating a 2D velocity profile. This velocity profile was then projected outwards onto the central and eastern transects, producing a velocity model for each profile which had vertical dimension depth sub-seafloor (Fig. 6).

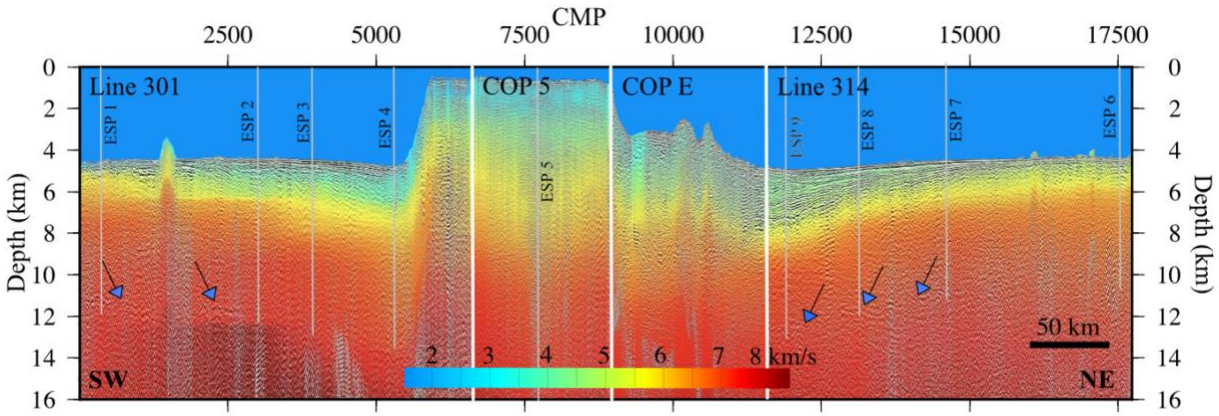

Figure 6. *P*-wave velocity versus depth model based on data from ESPs 1-9 (Figs. 3,4) superimposed on reprocessed Lines 301, COP 5, COP E and 314 which intersected the Hawaiian Ridge between Oahu and Molokai (Fig. 1). The velocity model was used to convert the two-way travel time seismic image to depth. Thin white lines locate the ESPs. Thick white lines separate reprocessed Lines COP 5 and COP E from composite Lines 301 and 314. Blue arrows delineate the reflection Moho.

To finalise the velocity model, all seismic data were migrated with a constant water velocity of 1500 m/s and water-bottom horizons were picked on the resultant images. The velocity models were then translated to beneath these water-bottom horizons and the water column flooded with a water velocity. In some cases, small seamounts were not considered in picking these water-bottom horizons to avoid artificial velocity pull-ups, as the main priority of this study was to image the top and bottom of oceanic crust in depth. The velocity profile for the western transect was created in the same way as the central and eastern transects, however ESPs 10 and 11 were used instead of ESP 5 in the model building process.

A combination of Kirchhoff Pre-stack time migration and angle stacking was used to create the final seismic images, whereby migration to 4 km offset with an aperture of 6 km was used into the oceanic crust, before merging with a stack from above the Moho to the end of the trace. This is because the structures visible above the oceanic crust were imaged best with migration while the Moho was imaged best by stacking, presumably because of the nature and strength of the noise at the depth of the Moho.

After this merging, post-stack processing was performed including gain enhancement in the frequency domain, F-K coherency filtering and a depth-dependent low-pass filter. The final step in the processing flow was converting the seismic images to depth using the respective ESP-derived velocity models.

We applied the processing flow outlined above to all lines with the following exceptions: COP E and COP 5 had demultiple by parabolic radon applied after SRMA. Lines 331 and 332 had an additional gap deconvolution applied to supplement their debubble. The depth conversion velocity for COP E was clipped to a maximum value of 5.2 km s^{-1} because we observed velocities that were too fast over what we considered to be mostly extrusive landslide material on the north flank of Oahu. The choice of 5.2 km s^{-1} was largely based on shallow igneous crustal velocities derived from a preliminary interpretation of Ocean Bottom Seismometer (OBS) data along *Langseth* Line 2 which also crossed the north flank of Oahu (Boston et al., 2019). In addition, Line 303, on the bulge southwest of Oahu, was converted to depth for comparison with IODP drill site horizons using an ESP velocity where all velocities greater than 2.5 km s^{-1} shallower than 5 km depth were set to 2.5 km s^{-1}. This allowed us to more accurately account for the varying depth of top of oceanic crust along the line while enabling the well tie.

Due to the lack of available field data for Line 330, we reprocessed the Line 330 legacy stack that is available from the Marine Geoscience Data System (MGDS) online data repository (https://www.marine-geo.org/index.php). The simple post-stack reprocessing flow for this line was merging the online navigation with the seismic, applying static corrections, applying a low-cut then depth-dependent low-pass filter, followed-by depth-dependent gap deconvolution. Finally, we performed post-stack Kirchhoff time migration then depth conversion using the ESP *P* wave velocity model.

Fig. 7 shows both the legacy and reprocessed seismic images of Line 303 from the flexural bulge southwest of Oahu, where sedimentary structures and Moho are clearer and have less ringing in the reprocessed data. This improvement is largely due to effective bubble pulse removal and filtering. Steeply dipping reflectors (e.g., on or near the sea floor) are also imaged better due to pre-stack migration. Fig. 8 shows the same types of improvements on Line 314, which crosses the northern moat of Oahu. A spectrum plot is also shown in Fig. 8, highlighting the improvements in frequency content due to debubbling, denoise, and filtering. These

improvements include broadening the spectrum, removing the low frequency energy surge indicative of the bubble pulse, and generally balancing the spectrum to bring out higher frequencies.

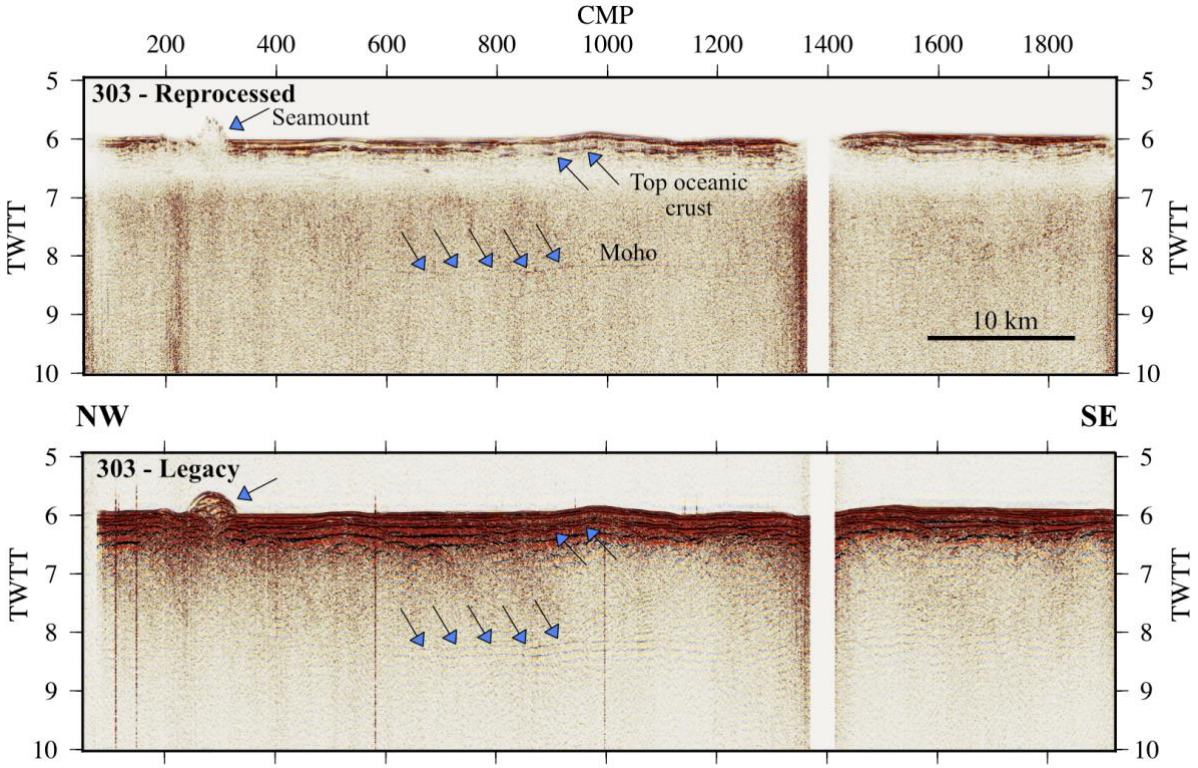

Figure 7. Reprocessed (top) and legacy (bottom) seismic images of Line 303 of the flexural bulge southwest of Oahu (Fig. 1). Improvements from reprocessing include a sharpened Moho, reduced ringing, and better-imaged sediment and top oceanic crust (blue filled arrows). The ringing below the top of oceanic crust (upper arrows) and Moho (lower arrows) in the legacy data is due to the bubble pulse, which was not removed during processing due to a difference in available technology. The improved imaging of the seamount (left-hand arrow) in the reprocessed data demonstrates the possible gains in imaging steep structures from migration.

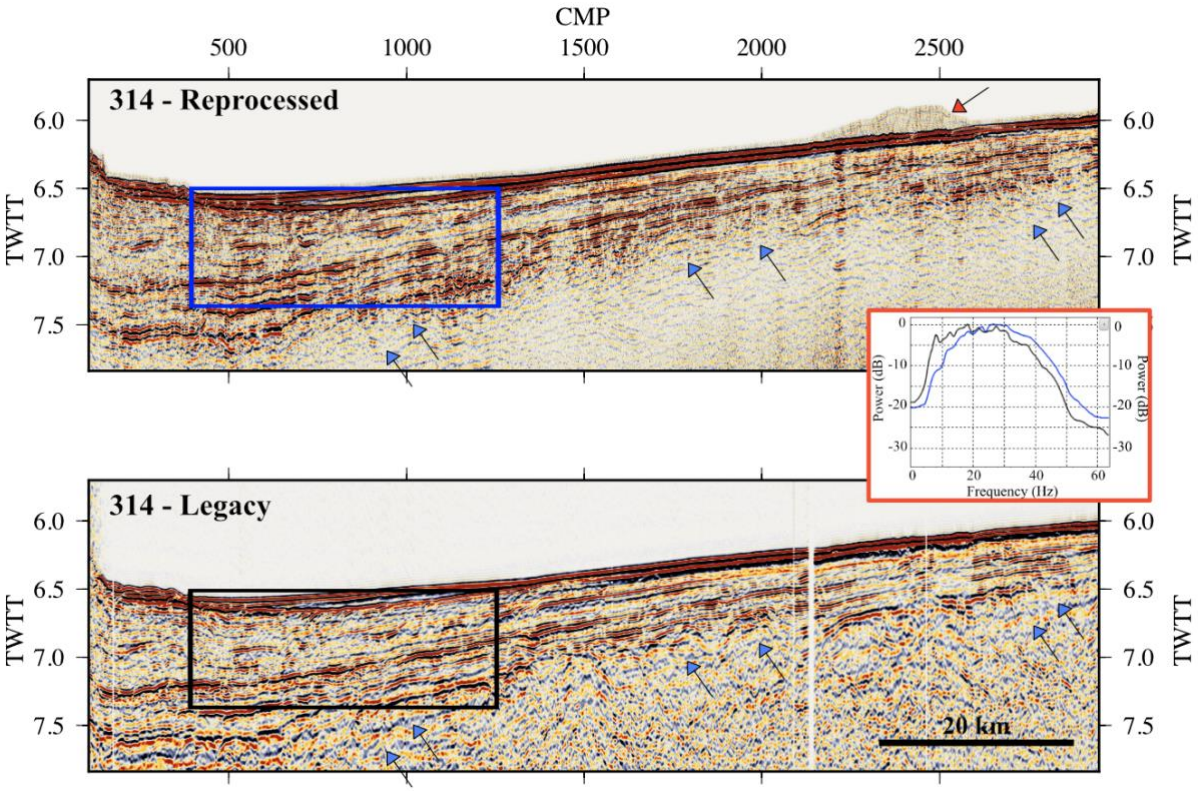

Figure 8. Reprocessed (top) and legacy (bottom) seismic images of Line 314 of the flexural moat northeast of Oahu (Fig. 1). Improvements from reprocessing include enhanced frequency content, reduced ringing, better-imaged sediment with more continuous strata, and a more clearly defined basement reflector. Inset shows a power spectrum of reflectors from the box region. The reduction and smoothing of the frequency spectrum between approximately 0 and 20 Hz is characteristic of an effective debubble, which corresponds to less high-amplitude ringing in the seismic data, seen dramatically in the lower left, middle and right side of the legacy data. The top of a seamount is imaged in the reprocessed data (red filled arrow) as, unlike in the legacy data, the reprocessed data is a composite dataset containing recordings from Lines 314, 317, 320, and 323; only one of which transited a seamount.

Fig. 9, which shows COP E (Line 313, Fig. 1), reveals the same general improvements as Figs. 7 and 8. In particular, we improve imaging of a reflector at ~6.5 - 7.5 s on the northeast flank of Oahu that we interpret as a décollement surface that separates the volcanic edifice from the top of the oceanic crust, similar to one identified by Morgan et al., (2003) from MCS data acquired on R/V *Ewing* on the south flank of Kilauea. The décollement connects directly to the base of the moat sediment and top of oceanic crust at approximately 7.5 s on CMP 2420. We note that migration noise from residual water bottom multiple is still present in the reprocessed data (approximately CMP 1500) and should not be interpreted as geological structure. Interestingly, COP E was not previously published nor used in prior flexure calculations. A structural interpretation of a depth converted representation of COP E Line 313 is shown in Supplementary Material (Fig. S1).

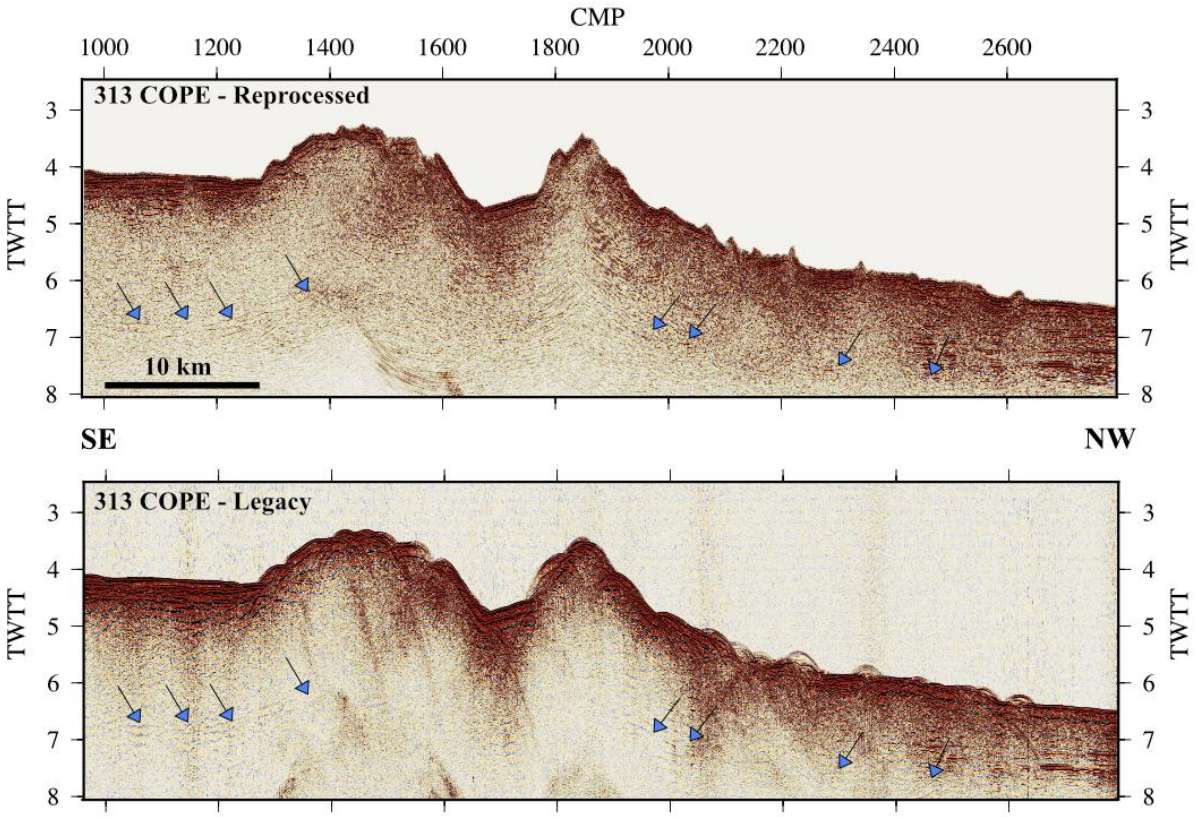

Figure 9. Reprocessed (top) and legacy (bottom) seismic images of Line 313 COP E which crossed the northeast flank of Oahu (Fig. 1). The flexural moat is just visible on the northwest end of the line. Improvements from reprocessing include a more visible and sharpened décollement reflector, reduced ringing, and better-imaged sediment and bathymetry. A mid-slope sedimentary basin is imaged in the reprocessed data between CMPs 1600 and 1800 and the improvement on seamount imaging along the line is notable. The moat sediment is visible on the lower right-hand side, where the base of this (i.e., the top of oceanic crust) becomes what we interpret as the décollement reflector, highlighted by blue arrows. Migration noise from residual water bottom multiple is seen in the reprocessed seismic at CMP 1500, TWTT 7.5 s.

Fig. 10 shows improved imaging of Line 330, which crosses the flexural moat southwest of Oahu, due to post-stack processing, as most of the line's field data was not available for pre-stack reprocessing. We focus on two small seamounts in the moat that highlight the benefits of post-stack time migration, including improved imaging of both sub-vertical structures and diffractors.

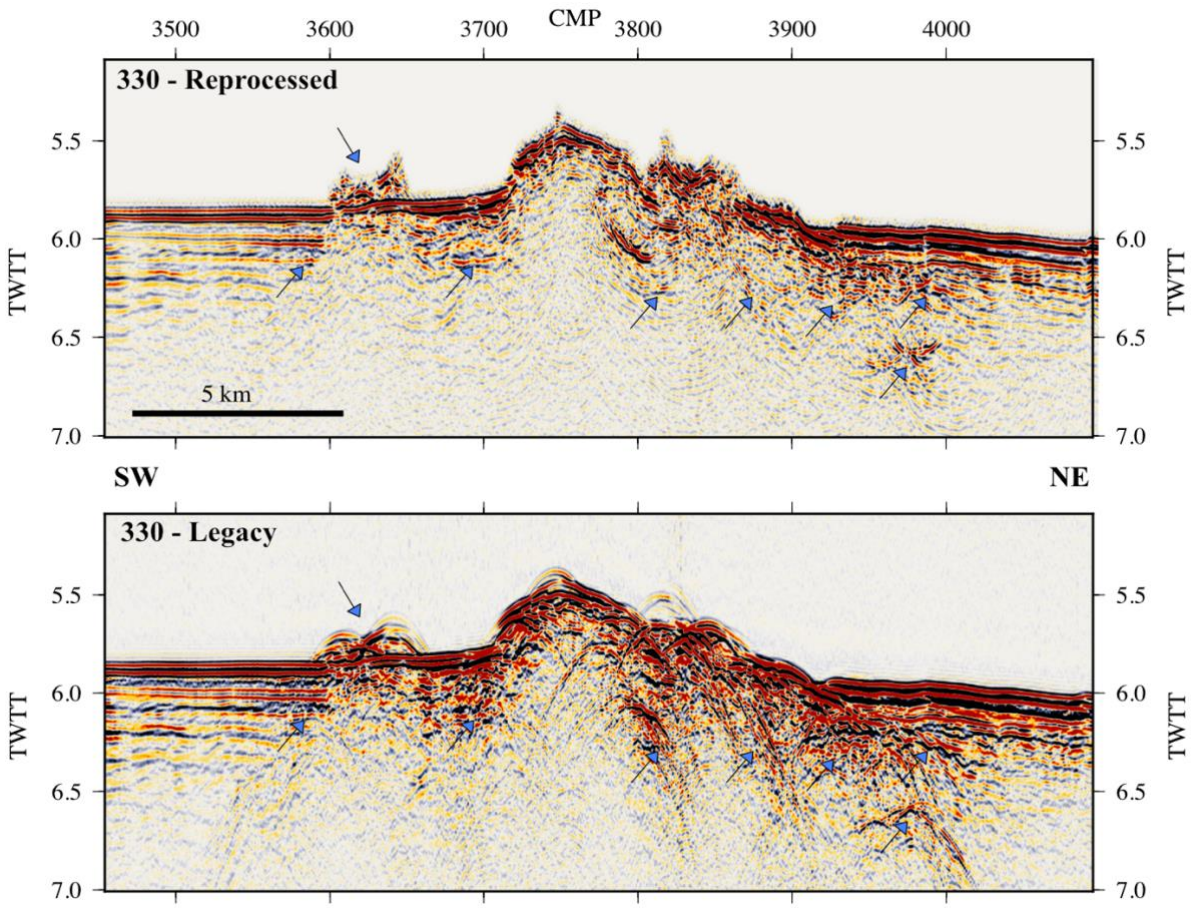

Figure 10. Post-stack reprocessed (top) and legacy (bottom) seismic images of Line 330 in the vicinity of two small seamounts in the flexural moat south of Oahu. Improvements from post-stack reprocessing include reduced ringing and very low frequencies, better-imaged sediment and bathymetry, and a clearer oceanic crust reflector. Segments of oceanic crust (blue arrows) and a possible deeper feature (CMP 3980, TWTT 6.6 s) are now interpretable between volcanic features after post-stack processing of the legacy data. An out-of-plane seamount is also more clearly imaged at CMP 3630 in the reprocessed data, while imaging is improved on steeply-dipping features as well.

Interpretation

The depth converted reprocessed RC2308 seismic data were subsequently loaded into the *Paradigm* seismic processing and interpretation software at Lamont-Doherty Earth Observatory, where we "picked" the top of oceanic basement, Moho, and a possible décollement surface separating the volcanic edifice from the top of oceanic crust. Picks of the reprocessed data were then verified by ODP drilling data at Site 843A/B and compared with picks on intersecting MGL1806 Line 2 (Fig. 1), and with the predictions of the structure of pre-existing Cretaceous Normal Polarity Pacific oceanic crust and simple elastic plate models of volcano loading in the vicinity of the Hawaiian Islands. Examples of the picks of top oceanic crust and Moho along the three long transect profiles (Fig. 1) are shown in Supplementary Material (Figs. S2-S4).

Fig. 11 shows a close agreement between the depth of the sediment/basalt contact at ODP Sites 843A and 843B (Shipboard Scientific Party, 1992) and the top of oceanic basement picks on RC2308 Line 303. The sediment/basalt contact at ~242 m and samples of basalt recovered at depths of ~262, ~288, ~297 and ~304 m confirm that our picks correspond to the top of oceanic crust and not a reverberant layer caused, for example, by younger deep-water volcanism. Sediment thickness varies little along the line, as expected for its orientation sub-parallel to the trend of the flexural bulge and moat southwest of Oahu. Sites 843A and 843B penetrated an upper yellow-brown clay layer which overlies a chert and nannofossil limestone layer and there is good evidence in the reprocessed data of a change in seismic facies at the depth of ~122 m (Orange horizontal bar in Fig. 11) that separates these two lithostratigraphic units.

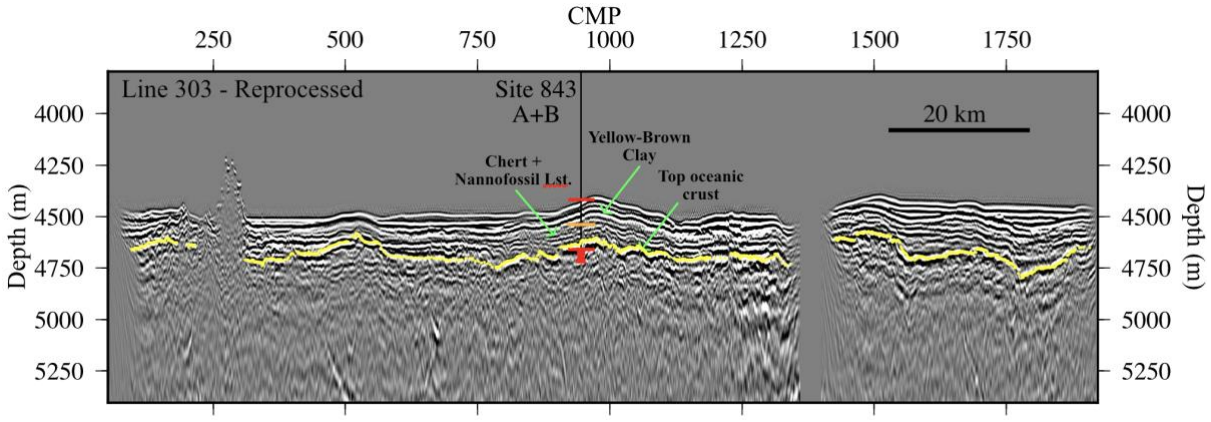

Figure 11. Interpretation of top of oceanic crust (yellow) along reprocessed Line 303 (see Figure 7). Ocean Drilling Project (ODP) drill sites 843A and 843B (Shipboard Scientific Party, 1992) sampled Yellow-Brown clay, Chert and Nannofossil Limestone and top of oceanic basement. Short orange line shows depth to the top of the Chert and Nannofossil Limestone. Yellow filled circles show the top of the oceanic basement as picked on the seismic data.

Fig. 12 compares the legacy and reprocessed picks along a line of projection centered on the southwest flank of Oahu: between Waianae volcano in the west and Koolau volcano in the east (dashed grey line, Fig. 1). The figure shows the picks of reprocessed data to be significantly smoother and less scattered than the original picks of legacy data, which we attribute to the application of modern processing techniques and to a greater accuracy of the digitisation of reflectors (picking was carried out digitally in the *Paradigm* software rather than manually on a light-table). Northeast of Oahu, the reprocessed picks reveal a remarkably smooth flexure of the top of oceanic crust that extends for distances of ~250 km from the flank of the volcanic edifice and to depths beneath it of up to ~4 km. Moho is not as well resolved, but the reprocessed data suggest that it too is flexed over a similar distance and depth.

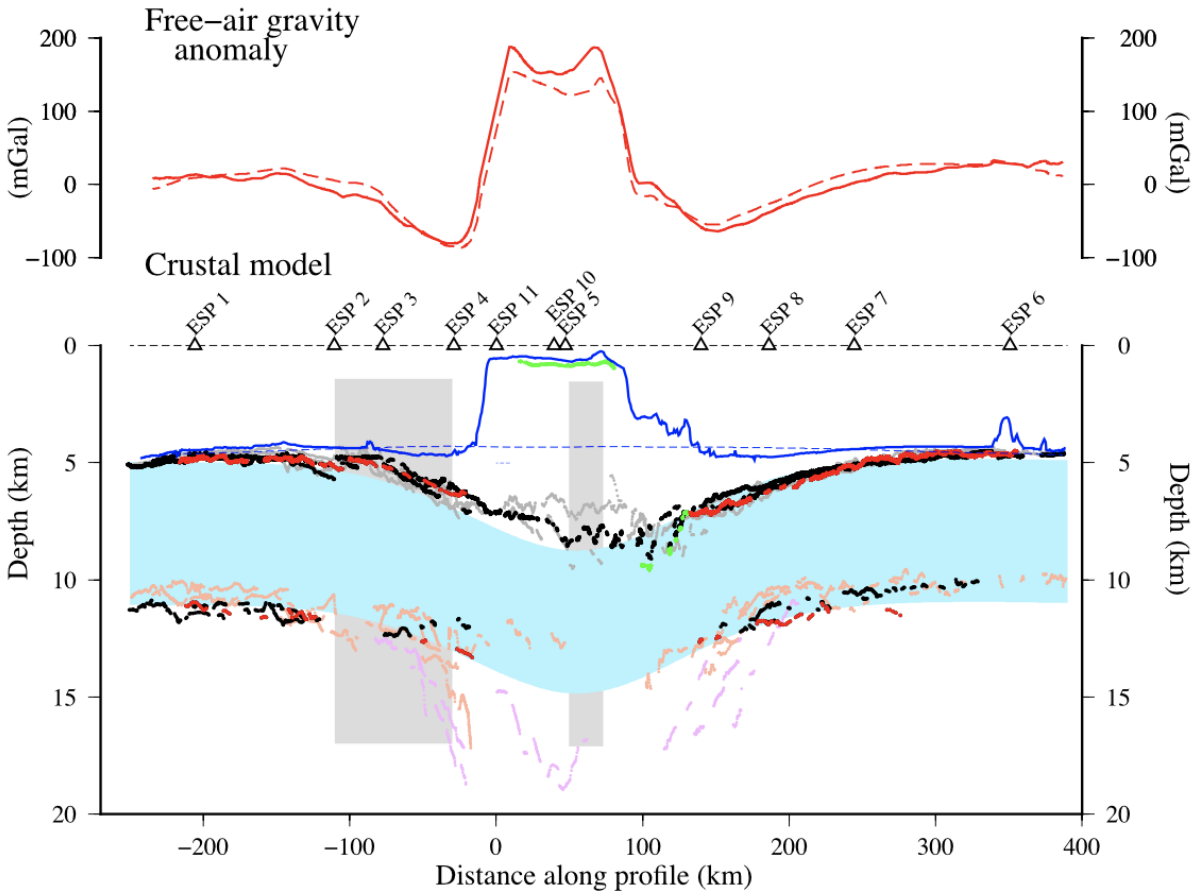

Figure 12. Comparison of the legacy and reprocessed reflector picks to the predicted top and base of oceanic crust based on a simple model of crustal structure and flexure. Red filled points show top and base of oceanic crust from the reprocessed two-ship data acquired along Lines 301 and 314. Black filled points show the same reflectors from the reprocessed single ship data acquired along Lines 330-332. Green filled points show reflectors from reprocessed data along COP 5 and COP E (Line 313, Fig. 1) which are interpreted as picks from within the edifice and its base respectively. Light coloured filled circles show the legacy picks associated with 'Reflectors 2, 3 and 4' (see Watts and ten Brink, 1989). Blue dashed line shows the Hawaiian swell crest obtained by median filtering (w=500 km) the bathymetry grid. The light blue shaded region and the dashed red line show the predicted crustal structure and gravity anomaly based on a simple model of flexure with surface (bathymetric) loading, elastic thickness, T_e, of 20.9 km and densities for the load, average infill, crust and mantle of 2737, 2418, 2800 and 3330 kg m^{-3} respectively. Grey filled boxes show where the multistranded Molokai Fracture Zone (MFZ) intersects the profile according to Mathews et al. (2011).

According to previous interpretations of legacy seismic reflection and ESP 5 velocity data (e.g., Watts et al. 1985; ten Brink and Brocher, 1987) and receiver function data (e.g., Leahy and Park, 2005; Leahy et al., 2010), flexed Pacific oceanic crust between Oahu and Molokai may be underplated by magmatic material, the upper and lower surfaces of which are at depths of ~14 and ~18 km respectively. The underplated material is intermediate in *P* wave velocity and density between lower crust and mantle and has been interpreted to represent melt that had ponded beneath flexed crust and subsequently cooled (e.g., Watts and ten Brink, 1989). However, we have found no evidence in the reprocessed reflection data for such an underplate. This is not to imply that the oceanic crust between Oahu and Molokai is not underplated, but

457 evidence needs to be established, not from reflection data, but from deep seismic refraction
458 data. Indeed, Lindwall (1988b) did not find any evidence of an intermediate velocity and
459 density layer from his modelling of ESP 5, preferring instead Moho at a depth of ~14 km. The
460 best evidence, however, will likely come from closely spaced OBS data such as that deployed
461 along Line 2 during the *Langseth* cruise since these data have the most potential to determine
462 the lateral changes in *P* wave velocities associated with such an underplate model (e.g., Dunn
463 et al., 2019).
464
465 Southwest of Oahu, the top of oceanic crust is not as smooth as to the northeast and
466 appears to be offset in the region of the Molokai Fracture Zone (MFZ) upon which the
467 Hawaiian Ridge has been emplaced. The MFZ is clearly visible in the satellite-derived gravity
468 anomaly field (e.g., Matthews et al., 2011; Sandwell et al., 2019), and these data show its
469 southern offset intersects the line of projection approximately between ESP 2 and ESP4 mid-
470 points while its northern offset extends toward a region between COP E and its intersection
471 with Line 331. The grey shade in Fig. 12 delineates the approximate extent of the two main
472 strands of the MFZ along the line of projection where there is evidence for a shallowing of the
473 top of oceanic crust by up to a few hundreds of metres and, possibly, a thinning of the oceanic
474 crust along both the western and eastern transects.

475 **Flexure modelling**

476
477 The picks of the top of oceanic crust from the RC2308 legacy and reprocessed data sets have
478 been used to re-assess the surfaces of flexure associated with the loading of the Hawaiian
479 volcanoes and the long-term mechanical properties of the Pacific oceanic lithosphere. The first
480 step was to estimate the elastic thickness, T_e, and the average infill density using a grid search
481 algorithm. Specifically, the observed picks are compared to the predictions of a simple 3D
482 elastic plate model in which the load is defined from a 1 × 1 minute GEBCO + SRTM 2020
483 bathymetric grid and a Young's modulus of 100 GPa, Poisson's ratio of 0.25, a uniform load
484 density of 2737 kg m^{-3}, a uniform density of the material that underlies the plate of 3330 kg m^{-3}
485 and a range of possible uniform elastic thickness (0 - 50 km) and average infill density values
486 (2100 -2800 kg m^{-3}) are assumed. After this, the best fit parameter pair that minimises the Root
487 Mean Square (RMS) difference between the observed picks and the calculated depth to the top
488 of oceanic crust is determined. These parameters were used as a central point about which a
489 Monte Carlo optimization scheme using the fast bounded simulated annealing algorithm was

employed to find the true best fitting parameters. Specifically, 1000 optimisations were run with uniform random starting points about the grid search solution, and all bounded simulated annealing solutions were then used as inputs into respective gradient descent routines to ensure a minimum had been found for every optimisation. The RMS plots produced by the initial grid-search routine (Fig. 13) show well defined minima and that reprocessing of the legacy data set has resulted in a significantly lower (by ~38%) RMS (Table 1, Rows 1 and 2).

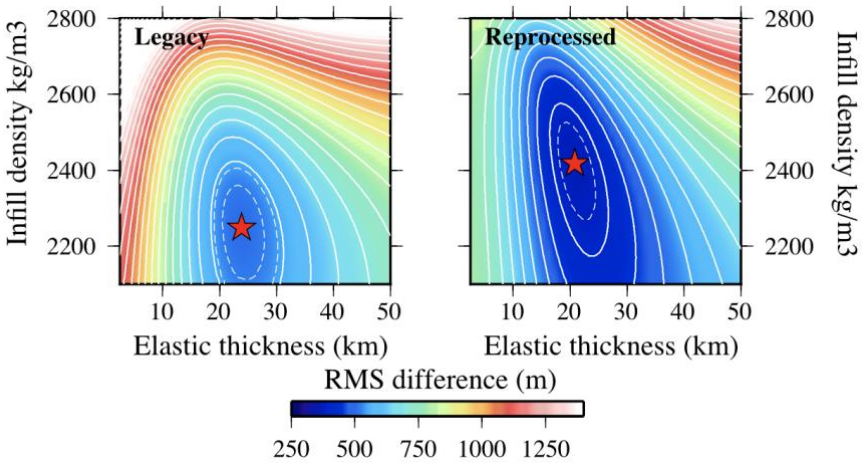

Figure 13. Comparison of the Root Mean Square (RMS) of the difference between observed and calculated depth to the top of oceanic crust. Observed depths are based on picks of the top of oceanic crust from the RC2308 legacy data and reprocessed data along Lines 301, 314 and 329-332. The calculated depths are based on a simple model of flexure with a surface (bathymetric) load defined by a 1 × 1 minute GEBCO 2020 bathymetry grid, an assumed load density of 2737 kg m^{-3}, uniform values of T_e in the range 0 - 50 km and average densities of infill in the range 2100 - 2800 kg m^{-3}. The red filled stars show the optimal misfit minima (Table 1).

Table 1

The Root Mean Square (RMS) difference between observed legacy and reprocessed data sets and the calculated depths to the top of oceanic crust based on a 3-dimensional simple elastic plate (flexure) model. Data in bold font are plotted in Fig. 12.

Data sets	Number of digitised picks	Elastic thickness, T_e (km)	Average infill density (kg m^{-3})	Top oceanic crust RMS (m)
RC2308 Legacy	4960	23.8	2249	511.2
RC2308 Reprocessed	**22369**	**20.9**	**2418**	**364.2**

The crustal structure corresponding to the T_e (20.9 km) and average infill density (2418 kg m^{-3}) that best fits the reprocessed seismic data picks of the top of oceanic crust (RMS =

364.2 m) is illustrated along the line of projection in Fig. 12 by the blue shaded region. Despite the good visual fit of the solution there are discrepancies. Most notable are in the region of the MFZ and beneath the edifice where the calculated depth to top of the oceanic crust is some 0.5 to 0.7 km deeper than the observed. There are also less obvious discrepancies in flanking moat regions where the wavelength of the calculated flexure appears too short compared to the observed.

The discrepancies in the seismic data are also manifest in the amplitude and wavelength of the free-air gravity anomaly. The RMS difference between observed and calculated gravity anomaly is 14.5 mGal. The calculated "high" anomaly over the edifice generally underpredicts the amplitude of the observed free-air gravity anomaly while the calculated "low" anomaly over the flanking moats is generally too short in wavelength compared to the observed. Both observations are suggestive of a higher elastic thickness and, possibly, a higher average infill density; we explore the impact of other factors on the estimated elastic thickness in the discussion.

Discussion

The flexure modelling and the reprocessing of legacy seismic data undertaken in this study provides the opportunity to obtain new insights into rheological properties of ~82.5-97.5 Ma Pacific oceanic lithosphere and to evaluate the scientific potential for undertaking such reprocessing on other similar legacy data sets.

Comparison with previous T_e values.

There have been a number of previous studies that have estimated the elastic thickness of the lithosphere, T_e, in the vicinity of the Hawaiian Islands (e.g, Gunn 1943; Walcott 1970; Watts and Cochran 1974; Watts 1978; Suyenaga 1979; Watts 1979; Kunze, 1980; McNutt and Shure 1986; Watts and ten Brink 1989; Wessel 1993; Zhong and Watts 2013). Of relevance to this study are the estimates of Watts and ten Brink (1989), Wessel (1993) and Zhong and Watts (2013), each of which were based on the RC2308 legacy seismic data set.

Watts and ten Brink, (1989) suggested the best fit to the top of oceanic crust reflector in the legacy data set was for T_e = 40 km and an average infill density of 2300 kg m^{-3}, assuming

548 a load density of 2800 kg m^{-3}, a Young's modulus of 100 GPa and a Poisson's ratio of 0.25.
549 The RMS difference between the observed depth to the top of the oceanic crust and the
550 calculated depth based on these parameters was 540 m. The study was based, however, on a
551 grid of 5 × 5 minute averages of shipboard single beam echosounder data offshore and a
552 ETOPO5 contour-derived data set onshore. Another problem was that the load was separated
553 assuming a uniform base of 4.5 km below sea level and so bathymetric features such as the
554 Hawaiian swell crest, landslide material and outlying seamounts were included in the load and
555 this together with its relatively high density assumed for the load suggest the load and hence
556 the T_e may well have been overestimated.
557
558 In this study, we have used a load based on a 1 × 1 minute GEBCO + SRTM 2020 grid
559 which incorporates a significant component of multibeam (swath) bathymetry data in addition
560 to the single beam data and so is of a significantly higher resolution than the one used in Watts
561 and ten Brink, (1989). Furthermore, the load was extracted using a base given by the mean
562 topography (5.019 km) and by masking out any flexural effects associated with landslide
563 material and outlying seamounts which may have formed in a different tectonic setting in
564 relation to the East Pacific Rise than the Hawaiian Ridge. The load density was also not
565 assumed but derived instead from a preliminary analysis of seismic refraction data acquired
566 along Line 2 (Dunn et al., 2019) to be 2737 kg m^{-3}. The resulting T_e of 23.8 and 20.9 km for
567 the legacy and reprocessed data sets respectively (Table 1, Rows 1 and 2) is significantly
568 smaller than that derived by Watts and ten Brink, (1989).
569
570 A final difficulty with the Watts and ten Brink (1989) study, pointed out by (Wesse
571 1993), was that it did not correct the depth to the top and base of oceanic crust for the effects
572 of the Hawaiian swell, a mid-plate bathymetric rise that has been attributed to an upwelling in
573 the mantle associated with the Hawaiian plume (Watts, 1976; Zhong and Watts, 2002), not to
574 plate flexure. Wessel (1993) used a best fitting "super-Gaussian" to remove the swell from the
575 legacy seismic data set and found T_e = 25 km which was significantly lower than that deduced
576 by Watts and ten Brink (1989) and an average infill density of 2550 kg m^{-3} which was
577 significantly higher. He also suggested spatial changes in elastic thickness with higher T_e north
578 of the northern offset of the Molokai Fracture Zone (~30 km) and lower T_e to the south (~20
579 km).
580

Although a relatively small effect because our line of projection mainly follows the crest of the swell, we followed Wessel (1993) and corrected both the legacy and reprocessed picks. We found that a simple median filter (w = 500 km) satisfactorily isolated the Hawaiian swell since tests showed that such a filter accounts well for both the flank and crest of the swell in the absence of the Hawaiian Island volcanic loads and their associated flexure (see thin dashed blue line in Fig. 12). The RMS plots for the swell corrected legacy and reprocessed seismic data produced by the initial grid-search routine show well-defined minima (Fig. 14). The best fit of T_e = 28.2 km and average infill density of 2547 kg m^{-3} (Table 2, Row 1) are in close agreement with the values deduced by Wessel (1993) from the same data set, but a different load geometry and density. The swell corrected reprocessed data set (Table 2, Row 2) suggests a slightly lower T_e (27.2 km) and higher average infill density (2625 kg m^{-3}) than the swell corrected legacy data set.

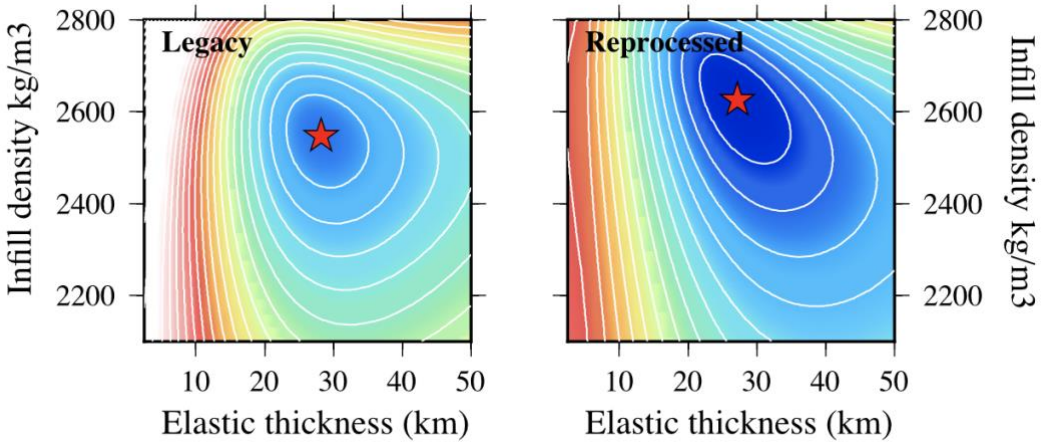

Figure 14. Comparison of the Root Mean Square (RMS) of the difference between observed and calculated depth to the top of oceanic crust. Observed depths are based on the same picks as in Fig. 12 but have been corrected for the effects of the Hawaiian mid-plate swell. The calculated depths are based on the same flexure model, load densities and ranges of infill density and T_e as in Fig. 12. The red filled stars show the optimal misfit minima (Rows 1-2, Table 2).

Table 2

The Root Mean Square (RMS) difference between observed legacy and reprocessed data sets and the calculated depths to the top of oceanic crust based on a 3-dimensional elastic plate (flexure) models. The observed data have been corrected for the effects of the Hawaiian mid-plate swell and the MFZ. Data in bold font are plotted in Fig. 15.

Data sets	Number of digitised picks	Elastic thickness, T_e (km)	Average infill density (kg m^{-3})	Top oceanic crust RMS (m)
RC2308 Legacy Swell corrected	4960	28.2	2547	503.1

RC2308 Reprocessed Swell corrected	22369	27.2	2625	412.1
RC2308 Reprocessed Swell + Isostatic corrected	**22369**	**26.7**	**2701**	**305.5**

606

607 We note that the RMS for the swell corrected reprocessed data (412.1 m, Table 2, Row
608 2) is not as low as might be expected; it is similar to the uncorrected data (364.2 m, Table 1,
609 Row 2). We attribute this to the main misfit in the data, which is associated with the region of
610 the MFZ, southwest of Oahu. The shallower top of oceanic crust in the MFZ is apparently
611 better accounted for in the reprocessed data by the low elastic thickness deduced from the
612 uncorrected data than the high elastic thickness deduced from the swell corrected data.
613
614 The top of oceanic crust systematically shallows in the MFZ by ~0.6 km which suggests
615 that it is unrelated to mechanical loading by the Hawaiian Islands since such loading would
616 induce more, not less, flexure than is observed. We are uncertain of the origin of the shallowing.
617 Recent age grids (Seton et al., 2020) suggest the seafloor in the vicinity of the MFZ is ~94 Ma
618 which should be 5684 m deep in the absence of a mid-plate swell according to the cooling plate
619 model. A shallowing of 0.6 km in the MFZ could therefore be indicative of younger seafloor.
620 However, this would require a seafloor age of ~54 Ma which seems unlikely. A more likely
621 explanation is crustal thickening due to magmatic addition. Irrespective, the shallower seafloor
622 would be expected to have been in some form of isostatic equilibrium prior to flexure. For
623 example, the observed shallowing of 0.6 km could be explained either by a Pratt-Hayford
624 model of isostasy with a compensation depth of 125 km and an average sub-crustal mantle
625 density 11.6 kg m^{-3} less than expected for 94 Ma oceanic lithosphere or by an Airy-Heiskanen
626 model of isostasy with a compensation depth at zero elevation of 31.2 km and crust that is 2.6
627 km thicker than expected.
628
629 Fig. 15 compares the reprocessed swell corrected picks that include an isostatic
630 correction in the vicinity of the MFZ to the predictions of the top and base of oceanic crust
631 based on a simple model of flexure. The optimal fit is for T_e = 26.7 km and an average infill
632 density of 2701 kg m^{-3} (Table 2, Row 3). The RMS difference between observed and calculated
633 depths is 305.5 m, which is ~26% lower than that without the isostatic correction. The RMS
634 was reduced even further (299.7 m) when account was taken of possible bias due to the
635 different number of picks in the edifice, moat, and bulge regions. The fit to the observed seismic

data along the line of projection is excellent (RMS = 338.4 m), as is the fit to the observed free-air gravity anomaly (RMS = 7.0 mGal) based on the 1 × 1 minute satellite-derived grid (V29.1) of Sandwell et al., (2019). We therefore consider the latter parameter pair as the optimum fit to the reprocessed *Conrad* seismic data.

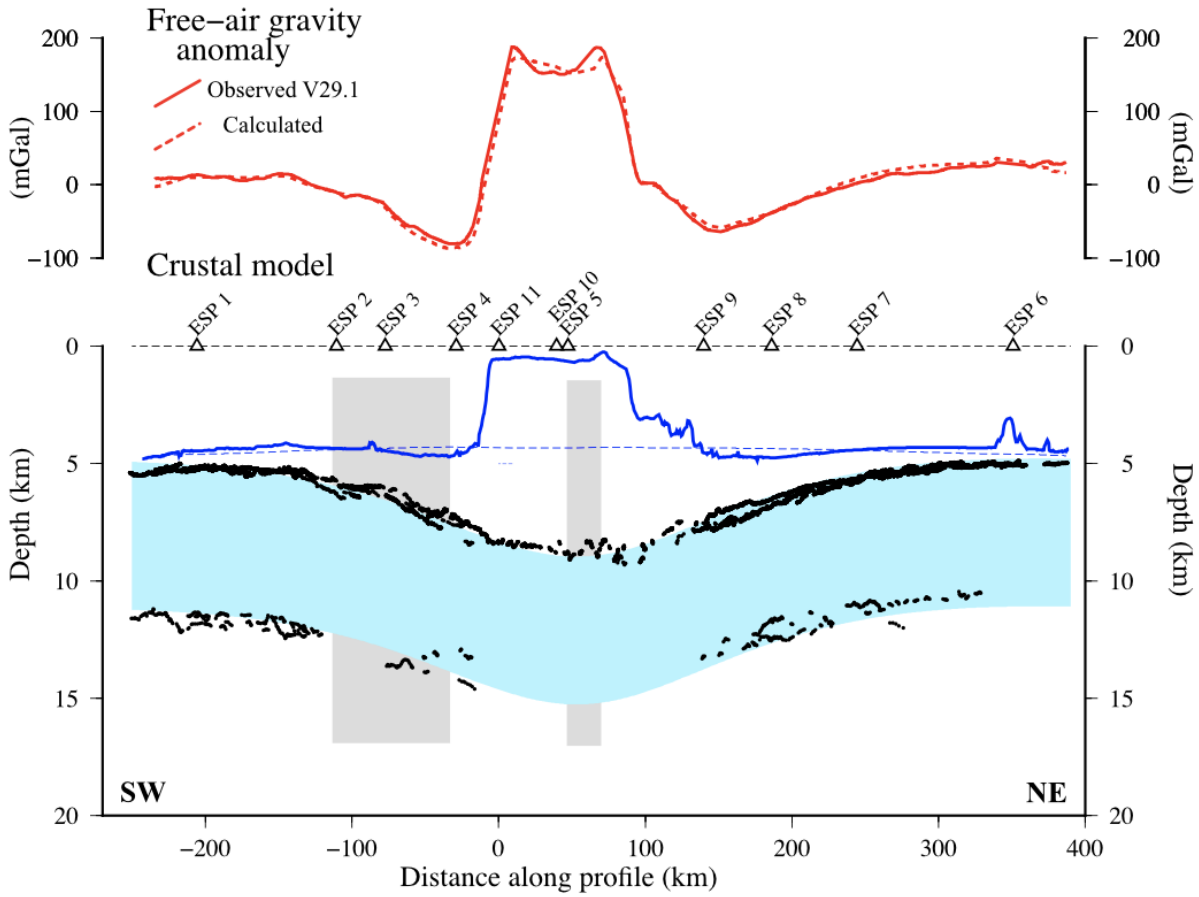

Figure 15. Comparison of the swell corrected and isostatically corrected reprocessed reflector picks to the predicted top and base of oceanic crust based on a simple model of flexure. Black filled points show picks along both the single ship and two-ship data. Dark blue dashed line shows the Hawaiian swell crest obtained by median filtering (w = 500 km) of the bathymetry grid. The light blue shaded region and the dashed red line show the predicted crustal structure and gravity anomaly based on a simple model of flexure with surface (bathymetric) loading, elastic thickness, T_e, of 26.7 km and densities for the load, average infill, crust and mantle of 2737, 2701, 2800 and 3330 kg m^{-3} respectively. The MFZ, shown in shaded grey, is defined in Fig. 12.

Variable load and infill densities

We have so far assumed a fixed load density (2737 kg m^{-3}) in the flexure calculations. As Minshull and Charvis (2001) and others have shown, load densities can impact the T_e estimate. Table S1 and Fig. S5 in Supplementary Material show the effect of different assumed load densities. Increasing the load density, for example, results in a higher T_e (by 1 km) and a lower infill density (by 40 kg m^{-3}). The reason for this is that increasing the load density results

658 in a larger flexure and so requires a higher T_e and smaller infill density to produce the same
659 depth to the top of oceanic crust. Decreasing the load density has the opposite effect and
660 requires a lower T_e (by 1 km) and higher infill density (by 50 kg m^{-3}). The RMS difference in
661 each case is, as expected, similar.
662
663 We also assumed that the infill density and hence the restoring force that acts on the
664 flexed plate is uniform and does not vary laterally from the bulges through the moats to beneath
665 the edifice. However, it is likely that the infill density will vary either side and beneath the
666 Hawaiian Islands. The bulge, for example, is an upward flexure that displaces water while the
667 region beneath the edifice is a downward flexure which is likely to comprise material with a
668 similar density to that of the load. The intermediate infill in the flanking moats is likely to
669 mainly comprise material derived from the edifice by mass wasting from the islands and hence,
670 depending on the amount of volcaniclastic material which may also infill the moats, to be lower
671 density than that of the edifice.
672
673 To investigate variations in infill density we compared the reprocessed swell corrected
674 data to the calculated flexure based on the 3-dimensional finite difference code of Cardozo and
675 Jordan (2001). We assumed the infill density beneath the load was the same as that of the load
676 and that the infill density in bulge regions (defined as a positive flexure) was water. We then
677 repeated the grid-search routine using the reprocessed swell corrected seismic data, but this
678 time searched for the best fit of T_e and the infill density in just the moat regions. The RMS
679 minimum (413.2 m) corresponds to a best fit T_e and moat infill density estimate of 24.3 km and
680 2550 kg m^{-3} respectively (Fig. 16). The infill beneath the edifice was 2737 kg m^{-3} and so the
681 average infill in this case would be 2643 kg m^{-3} which is similar to (but not the same as) the
682 value we determined previously using the same data set for the average infill density (2625 kg
683 m^{-3}). Therefore, the average infill density deduced in our optimal searches can be considered
684 approximately as an arithmetic average of the infill density beneath the edifice and the infill
685 density in the moats.

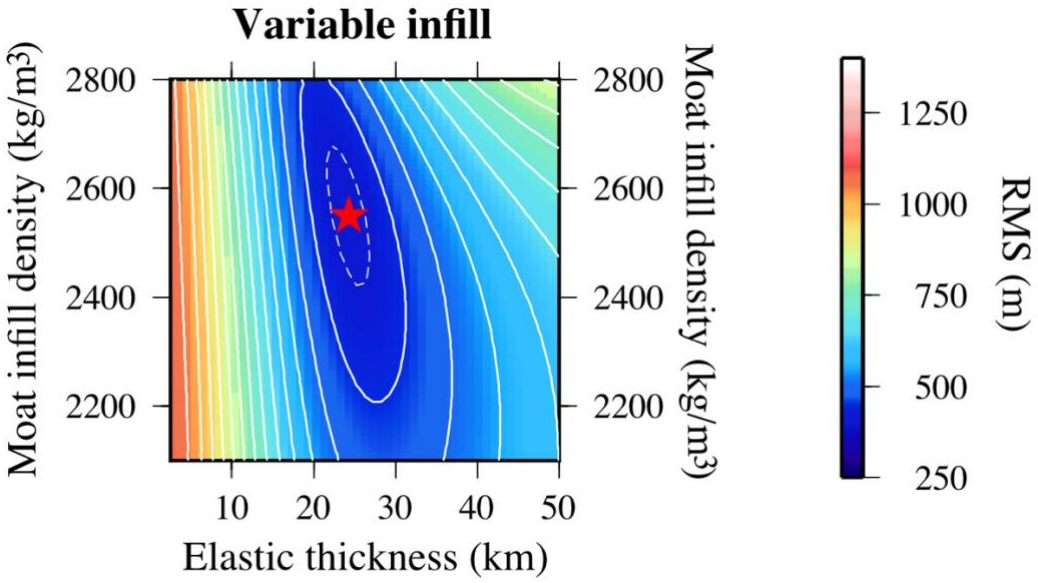

Figure 16. Comparison of the Root Mean Square (RMS) of the difference between observed and calculated depth to the top of oceanic crust using a variable moat infill density model. Observed depths are based on picks of the top of oceanic crust from the RC2308 reprocessed swell corrected data. The calculated depths are based on a finite difference model (Cardozo and Jordan,2001) with a surface (bathymetric) load defined by a 1 × 1 minute swath grid, assumed load density of 2737 kg m^{-3}, uniform values of T_e in the range 0 - 50 km and moat infill densities (vertical axis) in the range 2100 - 2800 kg m^{-3}. The RMS minimum (413.2 m) corresponds to a best fit estimate of 24.3 km and 2550 kg m^{-3} for the elastic thickness and the moat infill density respectively. The infill density inverted for using the swell corrected picks (Table 2, Row 2) of 2625 kg m^{-3} therefore appears to be approximately an average of the moat infill (2550 kg m^{-3}) and the infill assumed immediately beneath the edifice (2737 kg m^{-3}).

Comparison with Langseth Line 2

The *Conrad* MCS data were acquired with a relatively small air gun array and short streamer compared to that used during the *Langseth* cruise. It is instructive therefore to compare the two data sets.

Fig. 17 compares the *Conrad* reprocessed Line 303 and *Langseth* Line 2 data at the point of their intersection on the flexural bulge southwest of Oahu. The Moho is well defined in both MCS data sets where it appears to be represented by a single impulsive event. The profiles were acquired with two single ships, with one (*Langseth*) having a significantly larger volume airgun array and longer streamer than the other (*Conrad*) yet the visual character and frequency content of the Moho is strikingly similar in both data sets. We suspect this is due to the similar angle mutes used when imaging the Moho using both data sets, combined with similar depth-dependent bandpass filtering and the intrinsic frequency-dependent attenuation of the Earth. That is to say, the higher frequency components of the *Langseth's* airgun array are likely attenuated while travelling to the depth of the Moho and back to receivers, resulting

in an image of the Moho comparable in quality to that produced by *Conrad*. The top of oceanic crust and the overlying sedimentary structure, on the other hand, appears to be less well resolved in the *Conrad* data than in the *Langseth* data. We attribute this to the ringing in the *Conrad* data due to a residual bubble pulse and/or an untuned airgun array and to the higher frequency components of *Langseth's* tuned array.

The similarities and differences between the *Conrad* and *Langseth* MCS data sets are well seen in Fig. S6 of Supplementary Information which shows a normalized amplitude spectrum of a window of the data close to the point of intersection.

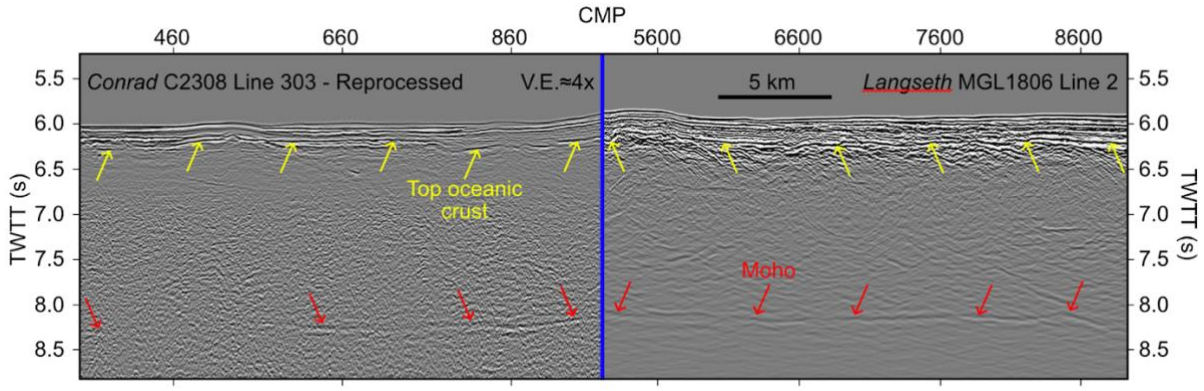

Figure 17. Comparison of a time section of *Conrad* RC2308 Line 303 and *Langseth* MGL1806 Line 2 at the point of their intersection (Blue solid line) on the flexural bulge southwest of Oahu (Fig. 1). Left-hand panel = *Conrad*. Right-panel = *Langseth*.

Implications for other Conrad data sets.

The reprocessing of the legacy data outlined in this paper and its successful application to a hotspot generated seamount chain in a plate interior has been based only the seismic data acquired during a single cruise RC2308 of *Conrad* in 1982. R/V *Robert D. Conrad* was involved, however, in many other seismic experiments in each of the world's oceans and their margins (Fig. 18). Notable examples were the surveys carried out by; Diebold et al. (1981) of the Venezuela basin - Cruises RC1904 and RC2103; Herron et al. (1978) and Detrick et al. (1987) of the East Pacific Rise at 9º and 13 ºN - Cruises RC2002 and RC2607; Ludwig and Rabinowitz (1982) of the Falklands/Malvinas Plateau and Trough - Cruise RC2106; Talwani et al., (1981) of the Norwegian Sea and Voring Plateau - Cruises RC2113 and RC2114; Holik and Rabinowitz (1991) of the Morocco passive margin - Cruises RC2405 and RC2406; Nissen et al. (1995) of the South China Sea passive margin - Cruises RC2612 - RC2614; White et al., (1990) of the Blake Spur Fracture Zone - Cruise RC2810, western Atlantic; Bangs and Cande

(1997) of the Chile active margin - RC2901 and RC2902; and Watts et al. (1990) of the Gulf of Valencia and Alboran Sea, Western Mediterranean – RC2911.

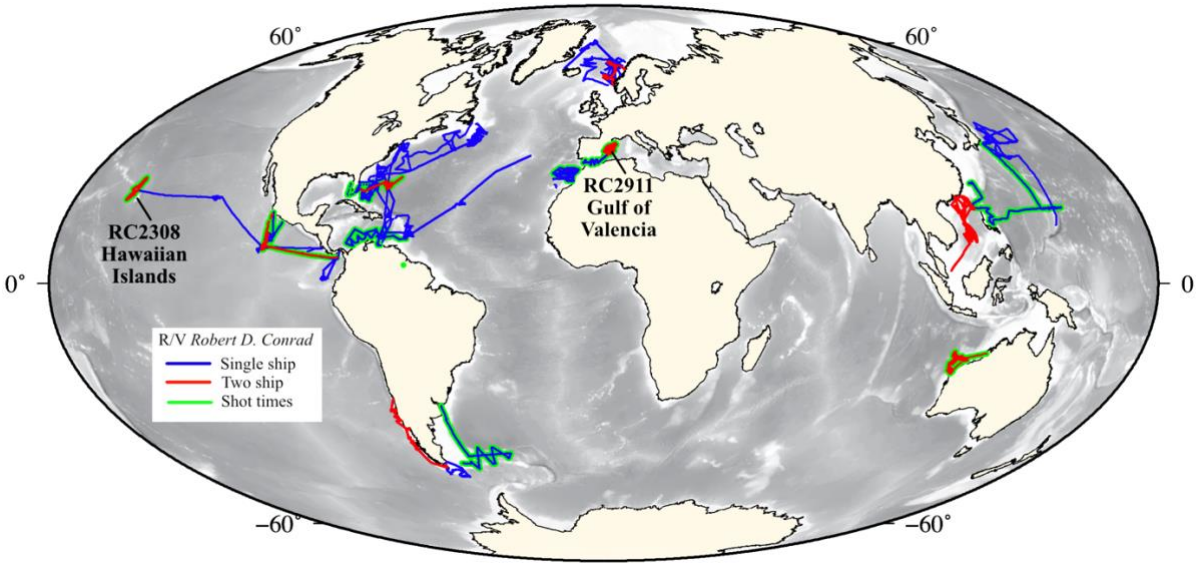

Figure 18. World map showing all the *Robert D. Conrad* single-ship and two-ship seismic cruises. Red = two-ship experiments. Blue = single ship experiments. Green = cruises with shot times that can be downloaded from the MGDS website. Cruises RC2308 and RC2911 were the first and last two-ship experiments that involved *Conrad*. Note that most seismic experiments of *Conrad* were focussed on the passive and active continental margins.

The wide range of geological features sampled - from mid-ocean ridges through oceanic plateaus to passive and active margins - suggest therefore that the seismic data from these cruises should be similarly reprocessed using modern processing algorithms such as those used here. We illustrate the benefits in Supplementary Information where we compare, in detail, segments of the legacy and reprocessed MCS data acquired during *Conrad* cruise RC2911 along Line 819 in the Gulf of Valencia (Watts et al., 1990) and MCS Line 827 in the Alboran Sea (Watts et al., 1993). Reprocessing (e.g., Figs. S9-S14) reveals new geological features not previously recognised in the RC2911 seismic data or reproduced in subsequent publications. These features include a set of steep faults which offset Plio-Pleistocene prograding deltaic sediments in the northern Gulf of Valencia, the internal structure of a stratigraphic unit bounded by unconformities that comprise the Messinian Erosional Surface in the southern Alboran Sea, and a lower continental crust that is characterized by “lamellae” rather than “crocodiles” and is underlain by a bright continuous Moho.

Conclusions

- Modern methods of processing of seismic data acquired during the 1982 single ship and two-ship *Conrad* RC2308 cruise to the Hawaiian Islands have significantly enhanced the value of this legacy data set, especially through the application of improved denoise, deconvolution, and migration technologies.

- Picks of reflectors on depth converted reprocessed data at the top of oceanic crust, within and at the base of the volcanic edifice, and Moho show them to be significantly smoother than the picks derived from the legacy data, for example, those used in Watts and ten Brink (1989) and subsequent rheological studies.

- The smoother picks result in a 38% reduction in the RMS difference between the observed reflector depths and the calculated depths based on analytical models of plate flexure and, hence, have yielded more reliable parameters for robust estimate of the elastic thickness and average infill density.

- A 2-parameter inversion of a swell-corrected reprocessed pick data set reveals a best fit elastic thickness, T_e, for the Hawaiian Ridge in the region of the islands of Oahu and Molokai of 26.7 km and an average infill density of 2701 kg m^{-3}. This parameter pair yields an RMS fit between the observed and calculated depth to top of oceanic crust and the observed and calculated free-air gravity anomaly of 305.5 m and 7.0 mGal respectively.

- Tests show our results to depend weakly on the load density assumed and that our estimates of the average infill density are, in fact, close to what would be predicted from an arithmetic average of the moat infill density and the density of the infill that underlies a volcanic edifice.

- The seismic reflection profile data acquired by the Lamont-Doherty Geological Observatory operated research vessel R/V *Robert D. Conrad* during 1975-1988 is an important legacy data set that may be used to re-examine not only the thermal and mechanical properties of oceanic lithosphere but also the structure, stratigraphy and evolution of the world's ocean basins and their margins.

Acknowledgements

This work was funded by a NERC grant NE/S01036X/1 and NSF grant OCE-2051501. We are grateful to ION Geophysical for reading the legacy 9-track seismic data tapes and for providing Lamont-Doherty Earth Observatory with access to the digital RC2308 legacy data prior to the R/V *Marcus G. Langseth* 2018 cruise and Joyce Alsop, Roseanne Weissel and Suzanne Carbotte for assistance accessing the data. We thank Shearwater Geoservices Ltd for provision of academic licences to run the *Reveal* seismic data processing software to Oxford and to Emerson for provision of academic licences to Lamont-Doherty Earth Observatory to the *Paradigm* processing and interpretation software suite. Figures were constructed using *Reveal* and GMT (Wessel and Luis, 2017) software.

Data availability statement

The reprocessed *Conrad* SEG-Y data used in this research are available for download from the Marine Geoscience Data System (MGDS) at https://www.marine-geo.org/tools/search/entry.php?id=RC2308 and in GeoMapApp (geomapapp.org). The data, which includes navigation in the SEG-Y headers, has been assigned a DOI of 10.26022/IEDA/331293. The field data for RC2308 will become available at the same URL before the end of the year.

References

Ayala, C., M. Torné, and E. Roca (2015), A review of the current knowledge of the crustal and lithospheric structure of the Valencia Trough Basin, *Boletín Geológico y Minero*, *126*, 533-552.

Bangs, N. L., and S. Cande (1997), Episodic development of a convergent margin inferred from structures and processes along the southern Chile margin, *Tectonics*, *16*, 489-503.

Boston, B., et al. (2019), Lithospheric structure across the Hawaiian-Emperor Seamount Chain from seismic wide angle reflection-refraction tomography, American Geophysical Union, Fall Meeting, Abstracts.

Brocher, T. M., and U. S. ten Brink (1987), Variations in Oceanic Layer 2 elastic velocities near Hawaii and their correlation to lithospheric flexure, *J. Geophys. Res.*, *92*, 2647-2661.

834 Cardozo, N., and T. Jordan (2001), Causes of spatially variable tectonic subsidence in the
835 Miocene Bermejo foreland basin, Argentina, *Basin Research*, *13*, 335-357.
836 Collier, J., P. Buhl, M. Torné, and A. B. Watts (1994), Moho and lower crustal reflectivity
837 beneath a young rift basin: results from a two-ship, wide-aperture seismic-reflection
838 experiment in the Valencia Trough (western Mediterranean), *Geophys. J. Int.*, *118*, 159-
839 180.
840 Detrick, R. S., P. Buhl, E. E. Vera, J. C. Mutter, J. A. Orcutt, J. A. Madsen, and T. M. Brocher
841 (1987), Multichannel seismic imaging of the axial magma chamber along the East
842 Pacific Rise between 9°N and 13°N, *Nature*, *326*, 35-41.
843 Diebold, J. B., P. L. Stoffa, P. Buhl, and M. Truchan (1981), Venezuela Basin Crustal Structure,
844 *J. Geophys. Res.*, *86*, 7901-7923.
845 Dunn, R. A., et al. (2019), Crust and mantle structure across the Hawaiian-Emperor Seamount
846 Chain from seismic wide-angle reflection-refraction tomography, American
847 Geophysical Union Fall Meeting, Abstracts.
848 Gunn, R. (1943), A quantitative study of isobaric equilibrium and gravity anomalies in the
849 Hawaiian Islands, *J. Franklin Soc.*, *236*, 373-390.
850 Herron, T. J., W. J. Ludwig, P. L. Stoff, T. K. Kan, and P. Buhl (1978), Structure of the East
851 Pacific Rise crest from multichannel seismic reflection data, *J. Geophys. Res.*, *83*, 798-
852 804.
853 Holik, J. S., and P. D. Rabinowitz (1991), Effects of Canary hotspot volcanism on structure of
854 oceanic crust off Morocco, *J. Geophys. Res.*, *96*, 12,039-012,067.
855 Kunze, A. W. G. (1980), On the flexural rigidity and effective viscosity of the lithosphere in
856 the Hawaiian area, *Tectonophysics*, *69*, T1-T8.
857 Lanaja, M. (Ed.) (1987), *Contibución de la exploración petrolifera al conoocimiento de la*
858 *geologia de Espana*, 465 pp., Instituto Geológico y Minero de Espana, Madrid.
859 Leahy, G. M., J. A. Collins, C. J. Wolfe, G. Laske, and S. C. Solomon (2010), Underplating of
860 the Hawaiian Swell: evidence from teleseismic receiver functions, *Geophys. J. Int.*, *183*,
861 313-329.
862 Leahy, G. M., and J. Park (2005), Hunting for oceanic island Moho, *Geophys. J Int.*, *160*, 1020-
863 1026; doi 1010.1111/j.1365-1246X.2005.02562.x.
864 Lewis, S. D., and D. E. Hayes (1989), Plate convergence and deformation, North Luzon Ridge,
865 Philippines, *Tectonophysics*, *168*, 221-237.
866 Lindwall, D. (1988a), Deep crustal structure under and near the Hawaiian Islands, 122 pp, Ph.
867 D. thesis, University of Hawaii.

868 Lindwall, D. A. (1988b), A two-dimensional seismic investigation of crustal structure under
869 the Hawaiian Islands near Oahu and Kauai, *J. Geophys. Res.*, *93*, 12,107-12,122.
870 Ludwig, W. J., and P. D. Rabinowitz (1982), The Collision Complex of the North Scotia Ridge,
871 *J. Geophys. Res.*, *87*, 3731-3740.
872 Maillard, A., A. Mauffret, A. B. Watts, M. Torné, G. Pascal, P. Buhl, and B. Pinet (1992),
873 Tertiary sedimentary history and structure of the Valencia Trough (Western
874 Mediterranean), *Tectonophysics*, *203*, 57-75.
875 Matthews, K. J., R. D. Müller, P. Wessel, and J. M. Whittaker (2011), The tectonic fabric of
876 the ocean basins, *J. Geophys. Res.*, *116*, doi:10.1029/2011JB008413.
877 McNutt, M. K., and L. Shure (1986), Estimating the compensation depth of the Hawaiian swell
878 with linear filters, *J. Geophys. Res.*, *91*, 13,915-13,923.
879 Minshull, T. A., and P. Charvis (2001), Ocean island densities and models of lithospheric
880 flexure, *Geophys J. Int.*, *145*, 731-739.
881 Minshull, T. A., R. S. White, J. C. Mutter, P. Buhl, R. S. Detrick, C. A. Williams, and E. Morris
882 (1991), Crustal Structure at the Blake Spur Fracture Zone From Expanding Spread
883 Profiles, *J. Geophys. Res.*, *96*, 9955-9984, doi:10.1029/91JB00431.
884 Morgan, J. K., G. F. Moore, and D. A. Clague (2003), Slope failure and volcanic spreading
885 along the submarine south flank of Kilauea volcano, Hawaii, *J. Geophys. Res.*, *108*,
886 doi:10.1029/2003JB002411.
887 Mutter, J. C., M. Talwani, and P. L. Stoffa (1984), Evidence for a thick oceanic crust adjacent
888 to the Norwegian margin, *J. Geophys. Res.*, *89*, 483-502.
889 Nissen, S. S., D. E. Hayes, P. Buhl, J. Diebold, B. Yao, W. Zeng, and Y. Chen (1995), Deep
890 penetration seismic soundings across the northern margin of the South China Sea, *J.*
891 *Geophys. Res.*, *100*, 22,407-422,433.
892 Pascal, G., M. Torné, P. Buhl, A. B. Watts, and A. Mauffret (1992), Crustal and Velocity
893 Structure of the Valencia Trough (Western Mediterranean) Part II: Detailed
894 interpretation of 5 Expanded Spread Profiles*,* *Tectonophysics*, *203*, 21-35.
895 Sandwell, D. T., H. Harper, B. Tozer, and W. H. F. Smith (2019), Gravity field recovery from
896 geodetic altimeter missions, *Advances in Space Research*,
897 doi:10.1016/j.asr.2019.09.011.
898 Seton, M., R. D. Müller, S. Zahirovic, S. Williams, N. Wright, J. Cannon, J. Whittaker, K.
899 Matthews, and R. McGirr (2020), A global dataset of present-day oceanic crustal age
900 and seafloor spreading parameters, *Geochemistry Geophysics Geosystems*,
901 doi:10.1029/2020GC009214.

902 Sheridan, R. E., L. Pastouret, and G. Mosditchian (1978), Seismic stratigraphy and related
903 lithofacies of the Blake-Bahama basin, in *Initial Reports of the Deep Sea Drilling*
904 *Project*, edited by Benson. W. E. and R. E. Sheridan, U.S. Government Printing Office,
905 Washington D.C.
906 Shipboard Scientific Party (1970), Western Alboran Basin - Site 121, in *Intial Reports of the*
907 *Deep Sea Drilling Project*, edited by W. B. F. Ryan and K. J. Hsu, pp. 43-89, U.S.
908 Government Printing Office, Washington D.C.
909 Shipboard Scientific Party (1992), Site 843, *Proceedings of the Ocean Drilling Program,*
910 *Initial Reports*, *136*, 65-99.
911 Stoffa, P., and P. Buhl (1980), Two-ship multichannel seismic experiments for deep crustal
912 studies., *J. Geophys. Res.*, *84*, 7645-7660, https://doi.org/10.1029/JB084iB13p07645.
913 Suyenaga, W. (1979), Isostasy and Flexure of the Lithosphere Under the Hawaiian Islands, *J.*
914 *Geophys. Res.*, *84*, 5599-5604.
915 Talwani, M., J. Mutter, and O. Eldholm (1981), The initiation of opening of the Norwegian
916 Sea, *Oceanologica Acta*, 23-30.
917 Taner, M. T., and F. Koehler (1969), Velocity spectra-digital computer derivation and
918 applications of velocity functions, *Geophysics*, *34*, 859-881.
919 Torné, M., G. Pascal, P. Buhl, A. B. Watts, and A. Mauffret (1992), Crustal and Velocity
920 Structure of the Valencia Trough (Western Mediterranean) Part 1: A combined
921 refraction/wide angle reflection and near vertical reflection study, *Tectonophysics*, *203*,
922 1-20.
923 ten Brink, U. S., and T. M. Brocher (1987), Multichannel seismic evidence for a subcrustal
924 intrusive complex under Oahu and a model for Hawaiian volcanism, *J. Geophys. Res.*,
925 *92*, 13,687-613,707.
926 ten Brink, U. S. (1986), Lithospheric Flexure and Hawaiian Volcanism: A Multichannel
927 Seismic Perspective, 219 pp, Ph. D thesis, Columbia University.
928 Vera, E. E., and J. B. Diebold (1994), Seismic imaging of oceanic layer 2A between 9°30'N
929 and 10oN on the East Pacific Rise from two-ship wide-aperture profiles, *J. Geophys.*
930 *Res.*, *99*, 3031-3041.
931 Walcott, R. I. (1970), Flexure of the lithosphere at Hawaii, *Tectonophysics*, *9*, 435-446.
932 Watts, A. B., and J. R. Cochran (1974), Gravity anomalies and flexure of the lithosphere along
933 the Hawaiian-Emperor seamount chain, *Geophys. J. R. Astr. Soc*, *38*, 119-141.
934 Watts, A. B. (1976), Gravity and bathymetry in the Central Pacific Ocean, *J. Geophys. Res.*,
935 *81*, 1533-1553.

936 Watts, A. B. (1978), An analysis of isostasy in the world's oceans:1. Hawaiian-Emperor
937 Seamount Chain, *J. Geophys. Res.*, *83*, 5,989-986,004.
938 Watts, A. B. (1979), On geoid heights derived from Geos 3 altimeter data along the Hawaiian-
939 Emperor Seamount Chain, *J. Geophys. Res.*, *84*, 3817-3826.
940 Watts, A. B., U. ten Brink, P. Buhl, and T. Brocher (1985), A multichannel seismic study of
941 lithospheric flexure across the Hawaiian-Emperor seamount chain, *Nature*, *315*, 105-
942 111.
943 Watts, A. B., and U. S. ten Brink (1989), Crustal structure, flexure and subsidence history of
944 the Hawaiian Islands, *J. Geophys. Res.*, *94*, 10,473-410,500.
945 Watts, A. B., M. Torné, P. Buhl, A. Mauffret, G. Pascal, and B. Pinet (1990), Evidence for
946 reflectors in the lower continental crust before rifting in the Valencia Trough, *Nature*,
947 *348*, 631-635.
948 Watts, A. B., J. Platt, and P. Buhl (1993), Tectonic Evolution of the Alboran Sea Basin, *Basin*
949 *Research*, *5*, 153-177.
950 Wessel, P. (1993), A re-examination of the flexural deformation beneath the Hawaiian Islands,
951 *J. Geophys. Res.*, *98*, 12,177-112,190.
952 Watts, A. B., and J. Mutter (2015a), Multi-Channel Seismic Shot Data from the Western
953 Mediterranean Sea acquired during the R/V Robert D. Conrad expedition RC2911
954 (1988), IEDA, doi:10.1594/IEDA/320898.
955 Watts, A. B., and J. Mutter (2015b), Multi-Channel Seismic Shot Data from the Western
956 Mediterranean Sea acquired during the R/V Robert D. Conrad expedition RC2911
957 (1988) with the R/V Jean Charcot participating, IEDA, doi:10.1594/IEDA/320902.
958 Wessel, P., and J. F. Luis (2017), The GMT/MATLAB Toolbox, *Geochemistry Geophysics*
959 *Geosystems*, *18*, 811-823, doi:10.1002/2016GC006723
960 White, R. S., R. S. Detrick, J. C. Mutter, P. Buhl, T. A. Minshull, and E. Morris (1990), New
961 images of oceanic crustal structure, *Geology*, *18*, 462-465.
962 Yilmaz, O. (2001), Seismic Data Analysis. 2027 pp. Society Exploration Geophysicists Books.
963 Zhong, S., and A. B. Watts (2002), Constraints on the dynamics of mantle plumes from uplift
964 of the Hawaiian Islands, *Earth Planet. Sci. Letts.*, *203*, 105-116.
965 Zhong, S. J., and A. B. Watts (2013), Lithospheric deformation induced by loading of the
966 Hawaiian Islands and its implications for mantle rheology, *J. Geophys. Res.*, *118*, 6025-
967 6048, doi:10.1002/2013JB010408